Tampere University

Paavo Mäkinen

FLUORENE-BASED HOLE TRANSPORT MATERIALS FOR HALIDE PEROVSKITE SOLAR CELLS

ABSTRACT

Paavo Mäkinen: Fluorene-based hole transport materials for halide perovskite solar cells
Master of Science Thesis
Tampere University
Master's Programme in Science and Engineering
November 2021

The finite nature of fossil fuels and the impending climate change scenario have clearly highlighted the need for clean and renewable energy sources. The vast amount of energy constantly radiating from the Sun to Earth could be harvested to ease this issue, but large-scale adoption requires a more cost-effective solar cell technology than the currently available. A rising star in this field are perovskite solar cells, which, in barely more than a decade, have led to an improvement in the power conversion efficiency from 3.8 % to 25.8 %. In addition to the impressive efficiency, perovskites bear the advantage of low material costs and solution-processed fabrication methods suitable for upscaling. These properties make perovskites an interesting field of research.

Perovskite solar cells do however have their drawbacks as well. Organic perovskites are notorious for degrading when exposed to external factors like moisture, with the lead-based materials used in highest performing cells posing a significant environmental and human health risk. Additionally, certain materials used in perovskite solar cells, notably in hole transport layer, are quite expensive and require dopants, which may accelerate the degradation of the perovskite itself.

Thus, the aim of this thesis was to study four novel fluorene-based hole transport materials, DC77, DC79, DC81, and DC83, which are simpler and cheaper to fabricate than conventional ones. The goal was also to utilize them without dopants in a mesoporous perovskite solar cell. The research consisted of hole transport material characterization, in addition to solar cell fabrication, optimization, and stability monitoring.

The best performance of the new substances was achieved with DC77, with the highest solar cell efficiency of 13.9 %. In contrast, the reference cells utilizing the widely known Spiro-OMeTAD material (upon dopants addition) reached up to 20 % efficiency. This lower performance of DC-based devices has been caused by the lower hole mobility and conductivity of the DC hole transporters compared to Spiro-OMeTAD. Despite this, DC77 and DC79 had fairly good photophysical properties, which means that these substances could achieve higher performance with suitable dopants. On the other hand, as for stability, the performance of DC-cells kept improving significantly for a week after fabrication. Thanks to this increase, the efficiency of the DC-cells mostly stayed above the starting value throughout the observation period of 147 days, unlike the reference cells which just gradually degraded to below 80 % of the initial value. Hence, the investigated fluorene-based hole transport materials have potential for the practical applications of perovskite solar cells, for which the long-term stability is paramount.

Keywords: Solar cell, photovoltaic, perovskite, hole transport material, fluorene

The originality of this thesis has been checked using the Turnitin OriginalityCheck service.

TIIVISTELMÄ

Paavo Mäkinen: Fluoreenipohjaiset aukonkuljetusmateriaalit halidiperovskiitti-aurinkokennoja varten
Diplomityö
Tampereen yliopisto
Teknis-luonnontieteellinen DI-ohjelma
Marraskuu 2021

Fossiilisten luonnonvarojen rajallisuus ja ilmastonmuutos ovat tehneet selväksi tarpeen ympäristöystävälliselle, uusiutuvalle energialle. Maapallolle säteilevä auringonvalo sisältää valtavan määrän energiaa, minkä hyödyntämiseksi jatkuvasti kehitetään yhä kustannustehokkaampia aurinkokennoja. Hieman yli vuosikymmenessä perovskiitti-aurinkokennot ovat kehittyneet 3,8 % hyötysuhteesta ilmiömäiseen 25,8 %. Hyötysuhteen lisäksi perovskiittien etuna on perinteistä piitä halvemmat raaka-aineet ja suureen skaalaan soveltuvat valmistusmenetelmät. Nämä ominaisuudet tekevät perovskiiteista houkuttelevia tutkimuksen kohteita.

Perovskiitti-aurinkokennoilla on kuitenkin myös omat ongelmansa. Perovskiittimateriaalit voivat hajota osa-aineiksen ympäristötekijöiden vaikutuksesta ja parhaimmat hyötysuhteet saavutetaan lyijypohjaisilla perovskiiteilla, jotka voivat hajotessaan aiheuttaa ympäristöongelmia ja terveysvaaran. Lisäksi tehokkaimmat aukonkuljetusaineet ovat kalliita ja vaativat douppausaineita, jotka voivat ennestään kiihdyttää perovskiitin hajoamista.

Näin ollen tämän diplomityön tavoitteena on tutkia neljää uutta fluoreenipohjaista aukonkuljetusainetta, DC77, DC79, DC81, ja DC83, joiden valmistaminen olisi huomattavasti yksinkertaisempaa ja halvempaa kuin nykyisten aukonkuljetusmateriaalien. Lisäksi tavoitteena oli saada nämä aukonkuljetusaineet toimimaan kennoissa ilman douppausaineita. Tutkimuksessa karakterisoitiin aukonkuljetusaineiden ominaisuuksia, sekä valmistettiin ja optimoitiin toimivia aurinkokennoja, tarkkaillen myös niiden stabiilisuutta.

Paras uusilla aukonkuljetusaineilla valmistettu aurinkokenno saavutti 13,9 % prosentin hyötysuhteen, kun taas muuten samanlainen kenno doupatulla Spiro-OMeTADilla antoi parhaimmillaan 20 %. Tämä ero vaikuttaisi johtuvan pääasiassa uusien aukonkuljetusaineiden heikommasta konduktiivisuudesta ja aukon liikkuvuudesta. DC77 ja DC79 osoittautuivat kuitenkin fotofyysisiltä ominaisuuksiltaan suotuisammiksi, joten sopivat douppaisaineet voisivat nostaa DC-aineiden suorituskykyä. Stabiilisuuden suhteen havainnoitiin mielenkiintoinen ilmiö, sillä DC-kennojen toiminta parani merkittävästi noin viikon ajan kennojen valmistuksesta. Tämän ansiosta DC-kennojen hyötysuhteet pysyivät 147 päivän tarkkailuaikana enimmäkseen alkuperäisten arvojen yläpuolella, toisin kuin referenssikennot, jotka laskivat alle 80 %. Näin ollen tutkitut fluoreenipohjaiset aukonkuljetusaineet voisivat toimia käytännön sovelluksissa, joissa pitkäaikainen stabiilisuus on tärkeintä.

Avainsanat: Aurinkokenno, perovskiitti, aukonkuljetusmateriaali, fluoreeni

Tämän julkaisun alkuperäisyys on tarkastettu Turnitin OriginalityCheck -ohjelmalla.

PREFACE

This work has been carried out in the Hybrid Solar Cells team of the Chemistry and Advanced Materials group at Tampere University under the supervision of Associate Professor Paola Vivo. I am grateful for this opportunity to work in the team and on such an interesting topic and would like to thank her for her guidance throughout this work. The co-examiner of this thesis was Postdoctoral researcher Arto Hiltunen, whose instruction, and help with the measurements has been invaluable. I would also like to thank both examiners for their patience in regard to my slow writing process.

Much of the characterization in this work would have been impossible without help from Postdoctoral Research Fellow Maning Liu, to whom I owe a debt of gratitude. I also want to thank my fellow Research Assistants Noora Lamminen, for showing me the ropes, and Sami Toikkonen, for assisting in the fabrication and measurement of latter solar cell batches.

My gratitude also goes to the entire Hybrid Solar Cells team and the people of the Redlabs, especially Laboratory Engineers Suvi Lehtimäki and Anna Railanmaa for their aid in complications involving the laboratory equipment. Naturally, I would also like to acknowledge Dr. Roberto Grisario at Politechnico di Bari in Italy for providing the very cornerstone of this work, the studied hole transport materials.

Last, but not least, I would like to thank my friends and family, for always supporting me and listening to my ramblings about work even when it made little sense to them.

Tampere, 14th November 2021

Paavo Mäkinen

CONTENTS

LIST OF SYMBOLS AND ABBREVIATIONS

ϵ_0	vacuum permittivity
ϵ_r	relative permittivity
μ_e	electron mobility
μ_h	hole mobility
ν	photon's frequency
ρ	resistivity
ρ_i	mass concentration
σ	electrical conductivity
A	area
c-TiO$_2$	compact titanium dioxide
CA	contact angle
CB	chlorobenzene
CsMAFA	Cs$_{0.05}$(MA$_{0.17}$FA$_{0.83}$)$_{0.95}$Pb(I$_{0.83}$Br$_{0.17}$)$_3$ perovskite
d	thickness of a semiconductor layer
DMF	*N,N*-dimethylformamide
DMSO	dimethyl sulfoxide
DSSC	dye-sensitized solar cell
$\overline{E}$	electric field
E_C	conduction band
E_G	band gap
EQE	external quantum efficency
ETL	electron transport layer
E_V	valence band
FA	formamidinium
FF	fill factor
FK209	tris(2-(1H-pyrazol-1-yl)-4-tert-butylpyridine)cobalt(III)-tris[bis(trifluoromethylsulfonyl)imide]

FTO	fluorine-doped tin oxide
h	Planck's constant
HOIP	hybrid organic-inorganic perovskite
HOMO	highest occupied molecular orbital
HTL	hole transport layer
HTM	hole transport material
I	electric current
I_D	current through a diode
I_P	current loss caused by shunt
I_{Ph}	photo-generated current
IQE	internal quantum efficiency
I_S	reverse saturation current
I_{SC}	short-circuit current
J	current density
J_{SC}	short-circuit current density
k	Boltzmann's constant
l	length of electrode
Li-TFSI	bis(trifluoromethane)sulfonimide lithium salt
LUMO	lowest unoccupied molecular orbital
m-TiO$_2$	mesoporous titanium dioxide
MA	methyl ammonium
MPP	maximum power point
n	diode quality factor
n_e	electron concentration
OSC	organic solar cell
p	hole concentration
P_{in}	power input to the cell
PCE	power conversion efficiency
PEDOT:PSS	poly(2,3-dihydrothieno-1,4-dioxin)-poly(styrenesulfonate)
PL	photoluminescence
PSC	perovskite solar cell
PTAA	poly[bis(4-phenyl)(2,4,6-trimethyl- phenyl)amine]

q	elementary charge
QDSC	quantum dot solar cell
R	resistance
R_C	contact resistance
R_L	lead resistance
R_P	shunt resistance
R_S	series resistance
SCLC	space-charge-limited current
SEM	scanning electron microscopy
SMU	source measure unit
Spiro-OMeTAD	2,2',7,7'-tetrakis(N,N-di-p-methoxyphenylamino)-9,9'-spirobifluorene
T	temperature
t	film thickness
TAU	Tampere University
tBP	4-tertbutylpyridine
TCO	transparent conducting oxide
TCSPC	time-correlated single photon counting
TRPL	time-resolved photoluminescence
UV-VIS	ultraviolet-visible
V	voltage
v_d	drift velocity
V_D	diffusion voltage
V_{OC}	open-circuit voltage

1. INTRODUCTION

With the advancement of technology, humanity's need for energy has continued to increase dramatically over the last century. In the face of finite resources and climate change it has however become apparent, that fossil fuels alone can no longer be used to satisfy these needs. The European Union has set the target for renewable energy at 32 % of energy end consumption by 2030 as part of the Renewable Energy Directive, with renewable sources becoming even more important in the long term goals. [1] To meet these demands it is necessary to continue researching new technologies to compete with the efficiency of traditional non-renewable energy sources.

While there are several sources of renewable energy, such as wind, geothermal, and hydropower, solar energy is one with great potential, that is still largely not utilized. The Earth receives approximately 10^5 TW of solar power, which would easily cover humanity's yearly electricity production of about 27 000 TWh in 2018 many times over. Although not all of that energy could obviously be harvested, the global solar energy production was a measly 554 TWh in comparison. [2, 3]

Thus, there is still room for improvement, even though solar cells have already found use in a multitude of applications, ranging from space stations to pocket calculators, and recently larger energy plants. Solar cell technologies can be divided into three generations. The first-generation cells are based on either mono- or polycrystalline silicon (Si) wafers and are capable of reaching high efficiencies, with industrial cells ranging between 14-20 % and record research cells reaching up to 26 %. [4, 5] However, the wafers are relatively thick, which makes the cells inflexible and adds to manufacturing cost. Even so the first generation still remain as the most common types of solar cells. [6] The second generation consists of thin film solar cells with materials such as amorphous silicon, cadmium telluride (CdTe), and copper indium gallium selenide (CIGS). They have lower efficiencies, but their active layer thickness is in the 1 μm range allowing for flexibility and they are typically more cost effective for small-scale applications. Finally, the third generation consists of a variety of emerging technologies, each with their own advantages and challenges. Third generation includes for example organic (OSC), quantum dot (QDSC), dye sensitized (DSSC), and *perovskite* (PSC) solar cells. [4] The focus of this thesis is on potential *hole transport materials* (HTM) to be used in perovskite solar cells and thus PSCs will be further explored in this text.

First, chapter 2 will cover the operational principles of photovoltaic cells, along with the unique qualities of perovskite solar cells and the requirements of their hole transport materials. Then chapter 3 will introduce the studied HTMs, together with the materials and methods used in this work. The obtained results will then be presented and discussed in chapter 4, with the final conclusions of this thesis taking place in chapter 5.

2. THEORETICAL BACKGROUND

This chapter will first discuss the basic theory behind the function of a solar cell, followed by the introduction of the parameters that describe its performance. Finally, the perovskite solar cell is given a more thorough introduction, along with its hole transport materials.

2.1 Basic principle of photovoltaic cells

A solar cell, or a photovoltaic cell is a device that converts light into electricity via the photovoltaic effect. At the bare minimum a solar cell is made up of a photoactive semi-conductor layer, sandwiched between two electrodes connected to an electrical circuit. One of the electrodes (typically the substrate as well) must be transparent for light to reach the active layer.

Semiconductors are materials with an electrical conductivity between that of insulators and full conductors. Their behaviour is based on energy bands and the gap between them. In a solid semiconductor crystal, the energy bands are formed from the limited energy levels of individual atoms packed closely together. These are the states that electrons can occupy in the material, with the most important ones being referred to as the *valence band* E_V and *conduction band* E_C. They are the highest occupied and the lowest unoccupied energy bands, which are analogous with molecular orbitals HOMO and LUMO in organic molecules respectively, and the difference between them is called the *band gap* E_G. In order for current to flow through the semiconductor, electrons need to be separated from the crystal lattice and lifted to the conduction band. [7]

In solar cells the required energy for this excitation is received from a photon of sufficient energy. When a photon with energy $h \cdot \nu > E_G$ (where h is Planck's constant and ν is the photon's frequency) is absorbed by the active layer, an electron is elevated to the conduction band. This creates an *electron-hole pair*. While the hole is merely an electron vacancy, it behaves as if it were a similar particle of positive charge. [7] This process is illustrated in Figure 2.1 in steps (a) and (b).

The formation of the electron-hole pair is however not sufficient alone for turning sunlight into electricity. Unless the electrons and holes are separated, they would eventually re-combine, and the energy would be lost in this relaxation. To prevent this the charges must
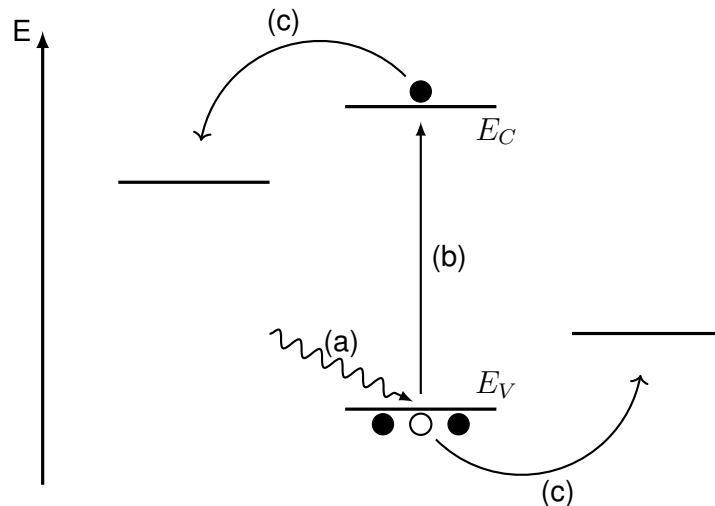
Figure 2.1. *Band diagram of a semiconductor, with steps demonstrating (a) photon absorption, (b) formation of an electron-hole pair, and (c) separation of charges towards the device electrodes.*

be driven towards the device electrodes. While applying an external electric field would separate the charges, it would not be beneficial for a device intended to generate electricity. In solar cells this driving force is usually considered to stem from an internal electric field achieved by doping semiconductors to create a junction, resulting in a strong internal electric field. [7] This field generates a so called drift current. There is also another type of current present in solar cells, the diffusion current, that occurs due to uneven distribution of charge carriers in the semiconductor material. [8]

The separated positive and negative charges are driven towards their respective electrodes, as depicted in Figure 2.1 step (c). The unbalanced charge creates a potential through the circuit connected to the solar cell, causing current to flow, until the electrons and holes are recombined. Thus, the total charge of the system remains constant, and the cell generates electricity through this circulation. [7]

2.1.1 Semiconductor doping and charge separation

The semiconductor can be doped by replacing atoms in its intrinsic crystal lattice with atoms that have more or less electrons than the primary semiconductor material. For example, a silicon atom has four valence electrons. Introducing a phosphorous (P) atom with five valence electrons into the silicon lattice would leave the fifth P electron unable to bond with surrounding silicon atoms. These excess electrons can then be easily elevated to the conduction band by a small amount of thermal energy, making the semiconductor more conductive via negative charge carriers. This is referred to as *n-type doping*, and the crystal lattice model has been presented in Figure 2.2a. The added dopant is in turn called a donor as it gives away an electron, gaining a positive charge in the process. [7]
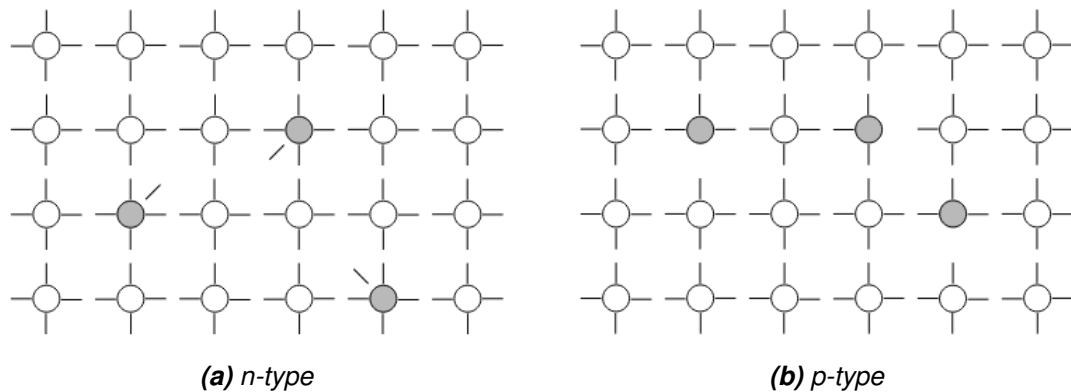
(a) n-type   *(b)* p-type

Figure 2.2. *Crystal lattice models of (a) n- and (b) p-type doping. The white circles present the primary semiconductor atoms, while grey circles present dopant atoms.*

Adding atoms with less valence electrons, such as boron (B) conversely leaves surrounding Si atoms without a bond, as the B atoms have only 3 valence electrons. This in turn engenders a hole in the crystal lattice, that can be filled by surrounding electrons causing the hole to move, acting as a positive charge carrier. Thus, the boron atom is called an acceptor and their addition is referred to as *p-type doping*. [7] Again, a model of the crystal lattice has been presented in Figure 2.2b.

In an n-type semiconductor most of the current is carried by the electrons in the conduction band, making electrons the majority carriers and holes the minority carriers. In a p-type semiconductor these roles are reversed, with holes in the valence band contributing the most to the current. The concentrations of these charge carriers are defined by the amounts of donor and acceptor atoms in the semiconductor. When a n-doped and p-doped semiconductor are joined together they form a *p-n-junction*. The majority carriers can then cross the junction as diffusion current and recombine with the opposite charges present on the other side. This results in a region surrounding the junction, where there are practically no free charges, but the donor and acceptor ions remain in the crystal structure as fixed charges. They create an electrical field $\overline{E}$, that opposes the diffusion current. Eventually the system reaches an equilibrium where the drift and diffusion currents are equal, and a space-charge region is formed around the p-n junction. This region causes a potential difference referred to as the diffusion voltage V_D, which allows holes from the n-side and electrons from the p-side to cross the junction. [7, 8] This system can also be illustrated via the energy bands of the p-n-junction as has been done in Figure 2.3. The energy bands bend together in the p-n-junction.

The p-n-junction opposes the movement of the majority charge carriers, but their flow can be controlled by applying a *bias voltage*. With a sufficiently high positive voltage from p to n the majority carriers from both sides can cross the boundary, overcoming the diffusion voltage. The applied voltage and the generated current are referred to as the forward voltage and current respectively. On the other hand, a negative voltage strengthens the
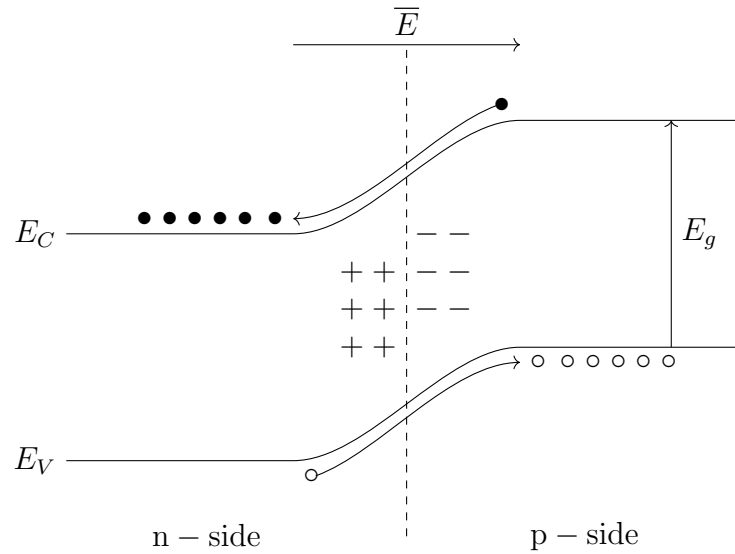
Figure 2.3. The energy band diagram of a p-n-junction. Electrons and holes are repre-
sented by black and white circles respectively, while the dashed line marks the junction,
surrounded by the space-charge region. E_g is the band gap between conduction (E_C)
and valence (E_V) bands. The fixed charges in the space-charge region create the electric
field $\overline{E}$.

space-charge region, effectively creating a barrier, that only a small amount of reverse
current can penetrate. [7, 8] This behaviour that is characteristic to semiconductor *diodes*
is further explored in the following subsection.

2.1.2 Characteristic current-voltage curve

Solar cells have a characteristic current-voltage (I-V) curve, which details their perfor-
mance at a specific voltage and current of operation. In dark it has similar shape to a
typical diode and ideally abides the general formula [7]

$$I_D = I_S(e^{qV/nkT} - 1), \tag{2.1}$$

where I_D is the current through the diode, I_S is the reverse saturation current, q is the
elementary charge, or $1.602 \cdot 10^{-19}$ A s, n the diode quality factor, $1 < n < 2$, k is the
Boltzmann's constant $1.381 \cdot 10^{-23}$ J K^{-1}, and T is operating temperature. Under illumi-
nation the shape remains mostly the same, but the photo-generated current I_{Ph} shifts
the curve from the first quadrant of the I-V plane to the fourth quadrant, where power is
produced. The total current in the cell is then

$$I = I_D - I_{Ph}. \tag{2.2}$$

A theoretical example of this behaviour is presented in Figure 2.4. The total current pro-
duced by the cell is negative like this, but it may also be presented as positive by changing
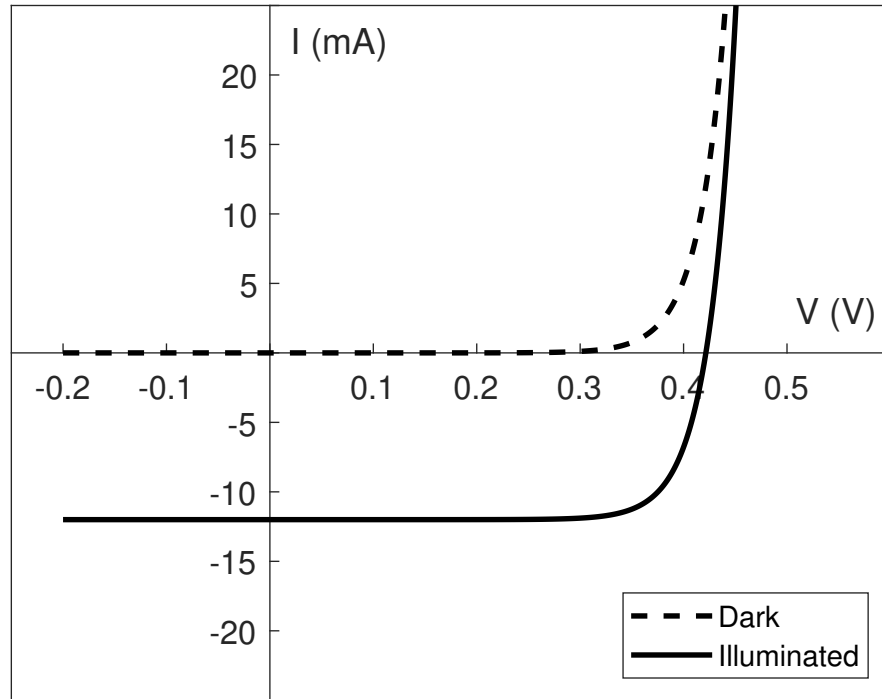
Figure 2.4. *Characteristic I-V curves of a theoretical solar cell drawn using Equations 2.1 (dashed) and 2.2 (solid line). The parameters used were $I_S = 10^{-9}$ A, $I_{Ph} = 12$ mA, $T = 300$ K, and $V \in$ [-0.2, 0.8]*

the signs of the individual currents. A real solar cell obviously does not perfectly follow Equation 2.1. This is due to nonideal resistances in the solar cell. Series resistance R_S is the combination of the resistances in and between the solar cell layers and it primarily causes the I-V curve to become less steep, or even reduces the produced current at higher values. Shunt resistance R_P on the other hand prevents undesired short circuits via alternate current paths in the cell, such as pinholes, which would result in power losses. This means that in an ideal solar cell R_P would be infinite. [7, 9] An equivalent circuit of a solar cell is presented in Figure 2.5.

Taking the resistances into account, Equation 2.2 then becomes

$$I = I_D + I_P - I_{Ph}. \tag{2.3}$$

It can be further expanded with equation 2.1 and by approximating $I_P = \frac{V+R_S I}{R_P}$ to [7]

$$I = I_S(e^{\frac{q(V+IR_S)}{nkT}} - 1) + \frac{V + IR_S}{R_P} - I_{Ph}. \tag{2.4}$$

While there are even more accurate models for photovoltaics than presented in Equation
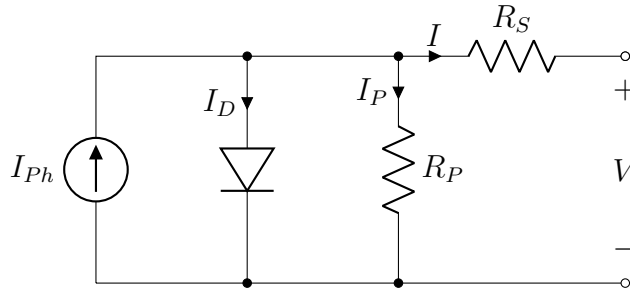
Figure 2.5. *A simplified equivalent circuit diagram of a solar cell, modeled with the series and shunt resistances (R_S and R_P, respectively).*

2.4 and Figure 2.5, it is sufficient to provide a basic understanding of solar cell behaviour. [7]

2.1.3 Solar cell parameters

Several important solar cell parameters can be easily obtained from its I-V curve. First, the short-circuit current I_{SC} and open-circuit voltage V_{OC} are the points of the curve where voltage is zero and current is zero, respectively. These are the maximum values of current and voltage that the cell can output. Short-circuit current density $J_{SC} = \frac{I_{SC}}{A}$ is often used instead of I_{SC} as it depends on the solar cell active area A, making it a better indicator of solar cell current production.

Next, the maximum power production of the cell P_{max} is obtained at the point where $P = I \cdot V$ reaches a peak, as illustrated in Figure 2.6. The point corresponding to this voltage on the I-V curve is referred to as the *maximum power point* (MPP). P_{max} can be used to calculate two important solar cell parameters, power conversion efficiency (PCE) and fill factor (FF) using the following Equations 2.5 and 2.6.

$$PCE = \frac{P_{max}}{P_{in}} \tag{2.5}$$

$$FF = \frac{P_{max}}{I_{SC}V_{OC}} \tag{2.6}$$

P_{in} is the the power of the light incident upon the solar cell, typically normalized to be equivalent to the power received from the sun. PCE is perhaps the most commonly used indicator of solar cell performance, providing a simple metric by which to compare different technologies. FF on the other hand describes the quality of the solar cell and can be seen as the "squareness" of the I-V curve.

All of the previously presented parameters examine the function of a solar cell under typical operational conditions, with the full spectrum of light. It is however also beneficial to analyze the efficiency of a solar cell at specific wavelengths, one wavelength at a time.
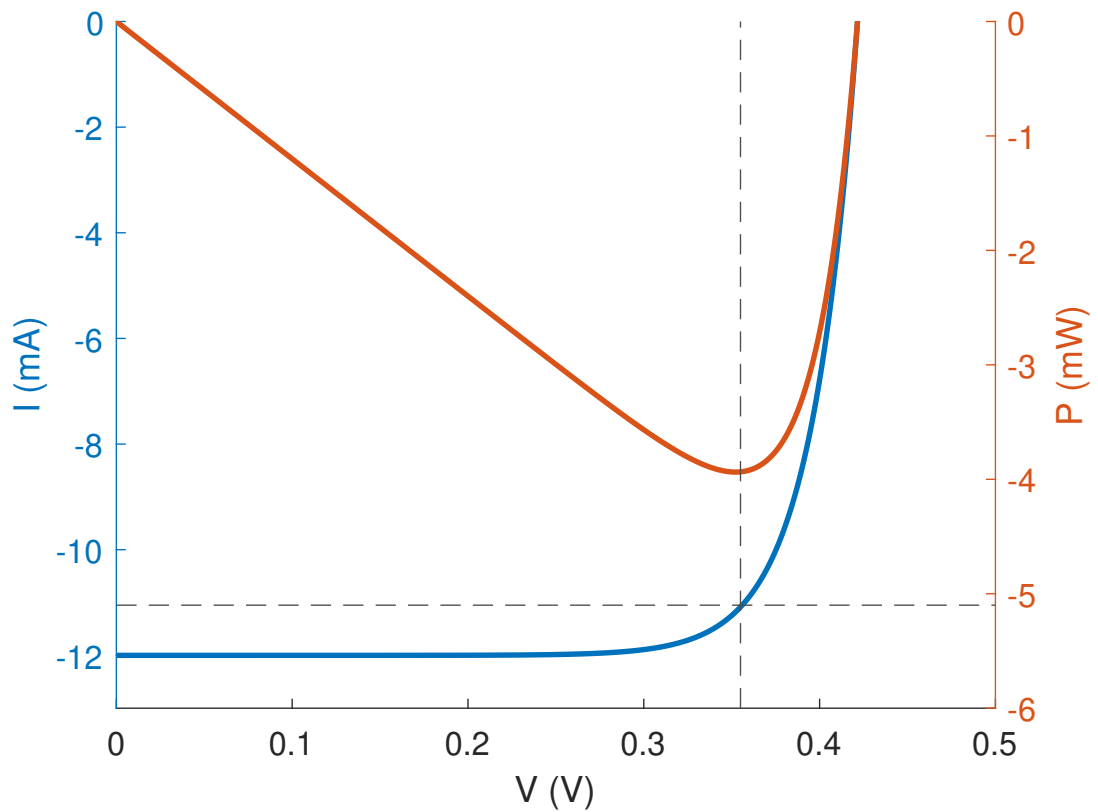
Figure 2.6. *The characteristic I-V curve of solar cell in blue drawn using the same parameters as figure 2.4, with the corresponding power of the solar cell plotted in red.*

This is due to the active layer of the solar cell only being capable of absorbing photons of energy greater than the band gap, and even then, not all photons can be converted to electricity due to losses. Conversion rate of photons to electricity at a certain wavelength can be expressed via *quantum efficiency*, of which there are two types: internal and external quantum efficiency (IQE and EQE respectively), defined as follows [10]

$$IQE = \frac{\text{collected electrons}}{\text{photons absorbed in the active layer}} \tag{2.7}$$

$$EQE = \frac{\text{collected electrons}}{\text{incident photons}}. \tag{2.8}$$

Thus IQE describes the absorption in the active layer, while EQE also shows losses from factors such as reflection and transmission, which also means that IQE is always larger. A high IQE means that the solar cell is able to effectively convert absorbed photons of that particular wavelength into electricity. [10]
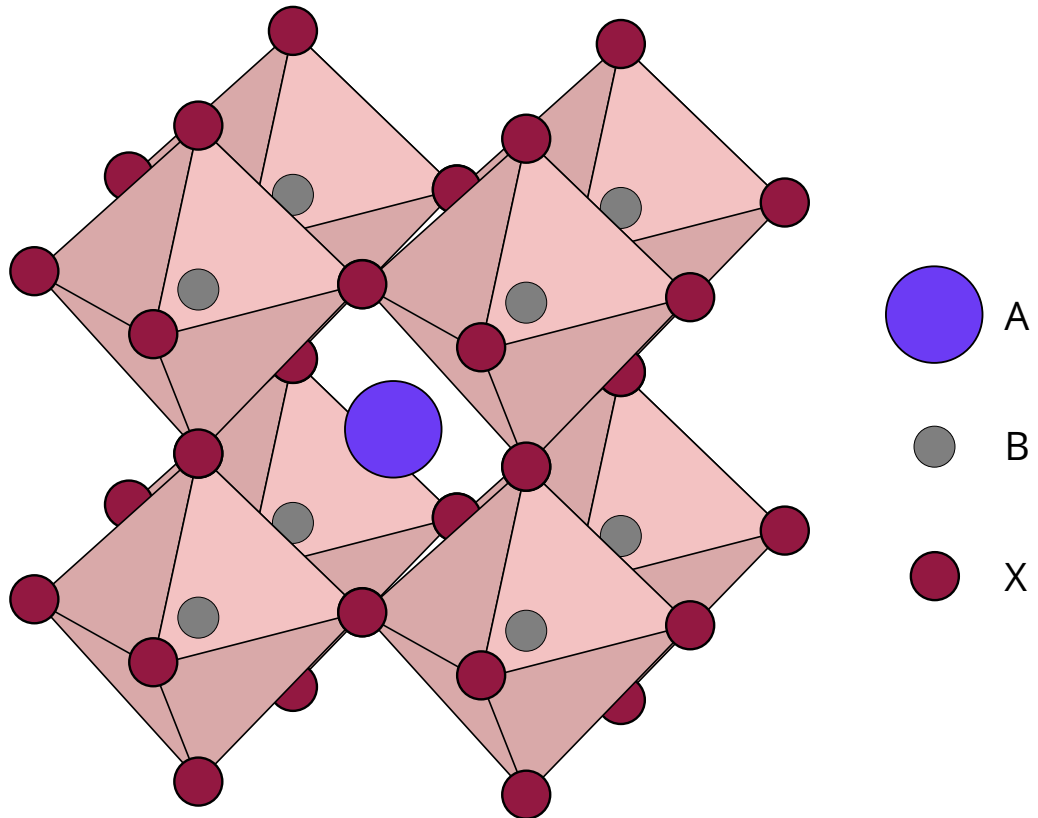
Figure 2.7. *A presentation of the cubic perovskite crystal structure.*

2.2 Halide perovskite solar cell

The term perovskite refers not only to a mineral composed of calcium titanium oxide ($CaTiO_3$) discovered in 1839, but also compounds that share the same crystal structure. This structure (illustrated in Figure 2.7) carries the general formula ABX_3, where A and B are large monovalent and small divalent cations respectively and X is an anion. While this classification would apply to a wide range of materials, photovoltaics commonly utilize *halide perovskites*, that may be hybrid organic-inorganic (HOIP) or completely inorganic. In this case, A is either the organic cation, such as methylammonium ion ($CH_3NH_3^+$, MA) and formamidinium ($HC(NH_2)_2^+$, FA) or a metal cation, e.g. cesium ion (Cs^+). B on the other hand is in both cases a metal cation, for example lead (Pb^{2+}) or tin (Sn^{2+}). Finally X is a halogen ion, typically iodide (I^-), bromide (Br^-) or chloride (Cl^-). [11] The perovskite may consist not only of three substances however, as mixed perovskites use various proportions of cations and anions, as is the case in the experimental part of this thesis.

While perovskites have been the topic of research for some time, PSCs are a very recent discovery. The first solar cells to utilize perovskites were reported by Kojima et al. in 2006 using $MAPbBr_3$ as a sensitizer on mesoporous titanium dioxide (titania, TiO_2) in a dye-sensitized solar cell structure, with a PCE of 2.19 %. [12, 13] In their initial work (2009) they also tested $MAPbI_3$, reaching a PCE of 3.81 %, although the solar cells decayed under illumination and air exposure. [14] Following their discoveries rapid progress was
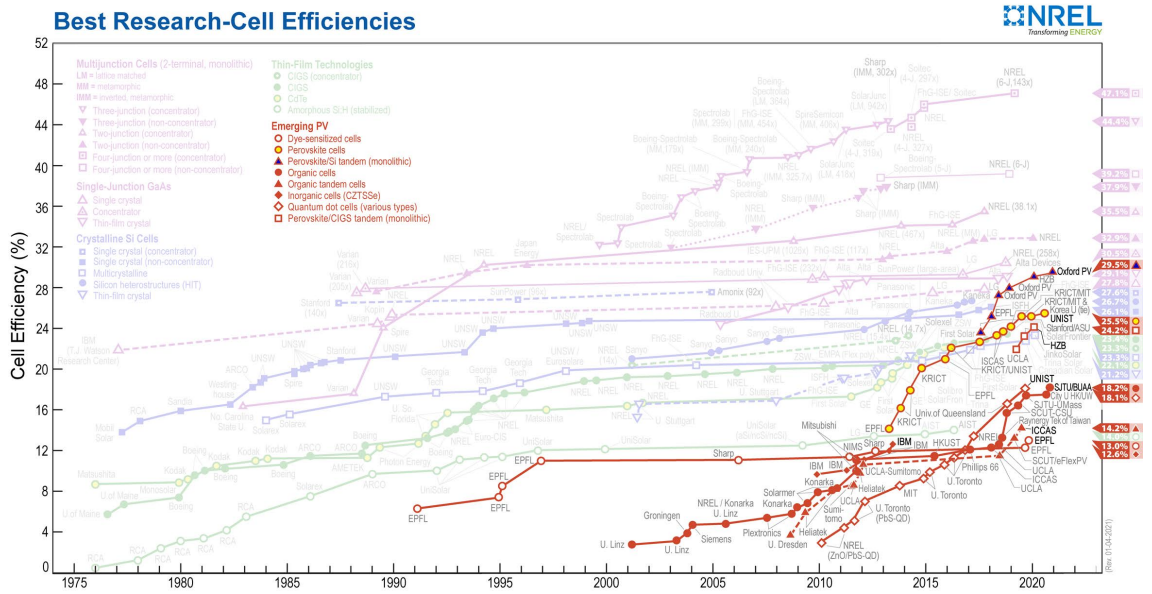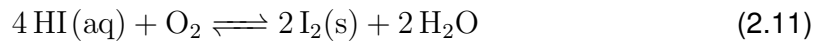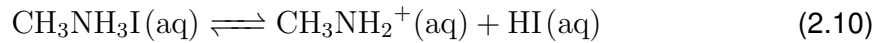
Figure 2.8. *Plot of state-of-the-art research solar cells with emerging photovoltaic technologies highlighted. Perovskite solar cells are marked by yellow dots with red outlines. This plot is courtesy of the National Renewable Energy Laboratory, Golden, CO. [5]*

made in a bit over a decade, with the current PCE record of 25.8 % (certified 25.5 %) under laboratory conditions. [15] Figure 2.8 presents the highest reached efficiencies of various solar cell technologies, clearly showing the swift ascension of PSCs. Factors that enable the high performance of of PSCs include strong optical absorption, excellent charge carrier transportation, tunable band gap, and tolerance to defects. [16]

Aside from the impressive efficiencies exhibited by PSCs, they also carry other advantageous qualities. First, they are thin-film solar cells, which means that they are lightweight and can be fabricated on polymer substrates to produce flexible solar cells for diverse applications. They are also made from materials that are available in vast quantities and can utilize solution-processed and thermal evaporation methods for fabrication, making cheap large-scale production viable. [16] Perovskites additionally have a potential application in *tandem cells* as a second photoactive layer, either alongside silicon, or with another perovskite. This is thanks to their tunable bandgap, which allows the combination of two photoactive layers with different band gaps to absorb a wider range of solar radiation. [17] These tandem cells can thus reach even higher efficiencies, with the current perovskite/Si tandem record at 29.5 %. [5]

Despite the impressive qualities of perovskite solar cells, they have their own issues. By far the greatest is the degradation of the cells over time. This is due to the perovskite materials used in solar cells having several phases, only some of which perform as efficient photoabsorbers. During the fabrication process, the perovskite is set in the most advantageous phase, but external factors, such as illumination, high temperature, moisture, and oxygen can cause this state to deteriorate. [18] Especially perovskites containing organic

cations, such as MA, are vulnerable to moisture degradation. An example of the chemical reactions in this degradation process has been presented in Equations 2.9-2.12. [19]

$$CH_3NH_3PbI_3(s) \rightleftharpoons PbI_2(s) + CH_3NH_3I(aq) \tag{2.9}$$

$$CH_3NH_3I(aq) \rightleftharpoons CH_3NH_2^+(aq) + HI(aq) \tag{2.10}$$

$$4\,HI(aq) + O_2 \rightleftharpoons 2\,I_2(s) + 2\,H_2O \tag{2.11}$$

$$2\,HI(aq) \rightleftharpoons H_2 + I_2(s) \tag{2.12}$$

The moisture degradation in this example involves HOIP, MAPbI$_3$ decomposing into aqueous MAI and the solid metal halide PbI$_2$ (2.9). MAI further breaking down (2.10) results in the formation of HI, which may react with oxygen to produce iodine and additional water (2.11), or decompose to hydrogen and iodine (2.12). Oxygen and increased temperatures can also accelerate the degradation of perovskite, while UV-light may for example induce a reaction between the perovskite and commonly used TiO$_2$. These issues rising from external factors can be alleviated by encapsulating the solar cell in a suitable material, but there are also intrinsic factors that affect PSC stability. These include defects, such as impurities and vacancies in the perovskite crystal structure and ion migration, that may cause reactions with surrounding materials. In order to counter both the external and intrinsic factors, a significant amount of research is dedicated to compositional and interfacial engineering, additives and fabrication techniques that would extend the lifetime of perovskite solar cells. [19, 20] The longevity of PSCs is vital for their large-scale implementation, as no matter how affordable they are to make, constantly replacing panels would raise the cost.

Another concern with perovskites is that the best performing materials use the toxic heavy metal, lead, which may be released during perovskite degradation. This has raised concerns over its use, as although the amount of Pb in a solar panel is less than a gram per square metre, careless large-scale adoption could have a drastic impact on both human health and the environment. Alternative metals have been experimented with, but they can't match the performance of Pb-based cells. Additionally, the best of these lead-free devices are often based on Sn, which is also a harmful chemical. [21] The other options, bismuth (Bi) and antimony (Sb) on the other hand have only provided PCEs below 4 % so far, compared to the tin PSCs, which can reach up to 14.6 %. [17, 22] In light of this performance difference, the most effective way of overcoming the toxicity issue seems to be the development of reliable encapsulation with Pb^{2+}-absorption materials, that would prevent any degradation products from leaking out. Naturally, proper protocols are also

necessary for manufacturing and disposal of the solar cells, but this is something that has already been done for example with lead-based batteries. [17, 21]

2.2.1 Solar cell structure

Perovskite solar cells are fabricated in various configurations, but there are three commonly used architectures: *mesoporous, conventional* (n-i-p) *planar* and *inverted* (p-i-n) *planar*. These structures are illustrated in Figure 2.9. The mesoporous PSCs evolved from the initial DSSC-type design of Kojima et al., where the perovskite was placed solely on the surface of nanocrystalline TiO_2 particles in a porous layer, to one that has a distinct layer of photoabsorbing perovskite. This perovskite layer partially blends with a mesoporous scaffolding that covers the electron transporting layer (ETL). The purpose of the scaffolding is to receive the diffusing electrons before they recombine, with the larger contact area also improving charge transfer. [23, 24] Both the scaffolding and the ETL commonly use TiO_2 or other metal oxides, for example zinc oxide (ZnO) and tin oxide (SnO_2). There are several properties that the ETL must possess, most notably good electron mobility μ_e, suitable energy levels to facilitate the electron transfer from the perovskite to the electrode and for blocking holes from advancing, along with high transparency and antireflection to allow light to reach the perovskite layer in a configuration where light passes through the ETL. [24]

In the mesoporous structure the bottom electrode (as illustrated in Figure 2.9), or cathode is a transparent conducting oxide (TCO), often fluorine-doped tin oxide (FTO). On the opposing side of the cell there is the compact hole transport layer (HTL) that inversely enables efficient hole transfer, while stopping electrons. The anode is typically metallic, with gold (Au) and silver (Ag) being common high-performance materials.

Planar solar cell architecture removes the mesoporous scaffolding in favour of simpler configuration and fabrication. This is possible thanks to the long carrier diffusion length and high charge carrier mobility of perovskites, which allow the electrons to cross the entire length of the perovskite layer. [23, 24] There are two types of planar PSCs, with the main difference between them being the order of the HTL (p) and ETL (n), and the intrinsic (i) perovskite layer. This designation stems from the semiconductor doping presented earlier and starts from the direction of incoming light. Thus, we have the conventional n-i-p structure (also seen in mesoporous cells) and the inverted p-i-n structure. The basic requirements for ETL and HTL remain the same in these configurations, except for the flipped transparency in p-i-n structure. [16]
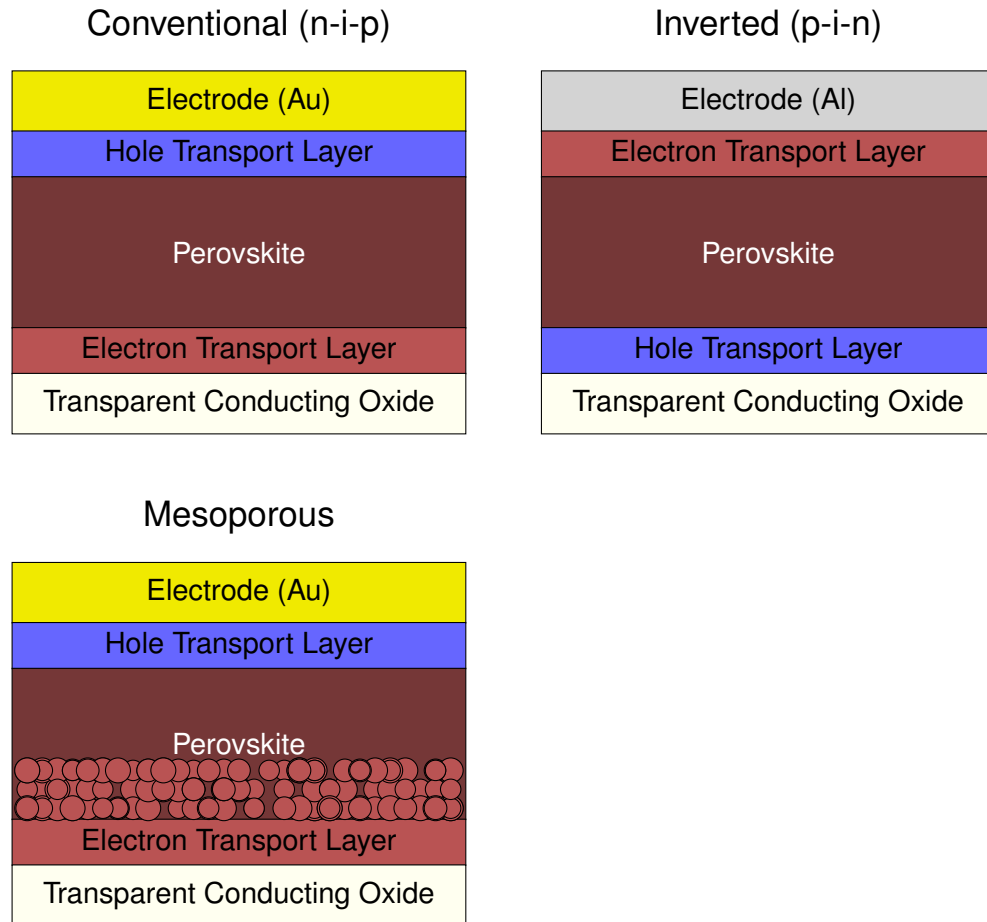
Conventional (n-i-p)

| Electrode (Au) |
| Hole Transport Layer |
| Perovskite |
| Electron Transport Layer |
| Transparent Conducting Oxide |

Inverted (p-i-n)

| Electrode (Al) |
| Electron Transport Layer |
| Perovskite |
| Hole Transport Layer |
| Transparent Conducting Oxide |

Mesoporous

| Electrode (Au) |
| Hole Transport Layer |
| Perovskite |
| Electron Transport Layer |
| Transparent Conducting Oxide |

Figure 2.9. *An illustration of three common PSC architectures. In this figure the light reaches perovskite through the bottom of the cells.*

2.2.2 Hole transport layer

As stated earlier, the purpose of a hole transport layer in a solar cell is to transfer holes to the anode of the solar cell and to block the passage of electrons. Naturally this means the HTL must possess a HOMO suitably close to that of the valence band of the absorbing layer, in order for the hole to be transferred (see Figure 2.1). To stop electrons the HTL should also have a LUMO higher than the conduction band of the perovskite. Aside from the energy levels that enable hole transfer between the layers, it is also important that the HTL can efficiently move the holes within itself. [16] This property is expressed in hole mobility μ_h, defined by the equation [25]

$$\mu_h = \frac{v_d}{E},\tag{2.13}$$

where v_d is the average drift velocity attained by the hole in an electric field E. Electron mobility μ_e can be calculated in a similar manner. Mobility describes the motion of the charge carriers in the semiconductor and it is also connected to conductivity σ which can
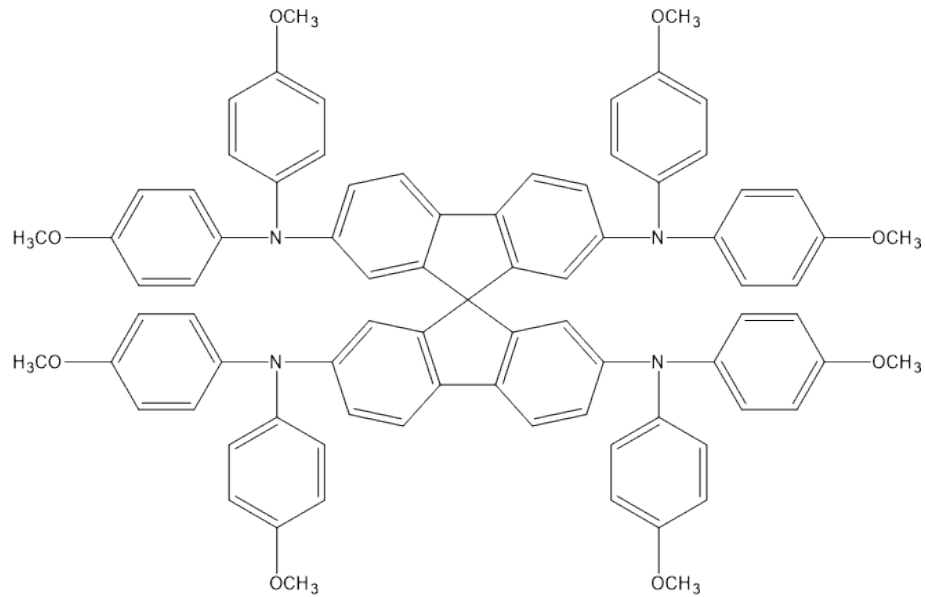
Figure 2.10. *The structural formula of a commonly used HTM, Spiro-OMeTAD.*

be expressed as [25]

$$\sigma = e(n_e\mu_e + p\mu_h),\tag{2.14}$$

where e is the elementary charge carried by holes and electrons, while n_e and p are electron and hole concentrations in the material, respectively. Therefore, σ is more directly related to the current that can flow through the semiconductor. In an HTM holes should be the majority contributor to σ, and vice versa. Good conductivity has been shown to improve the FF and V_{OC} of the cell, although lower values of σ can be alleviated by making the HTL thinner. [26, 27]

In addition to excellent charge transportation properties, a HTL should also possess great thermal and photochemical stability, to not deteriorate under continuous use. It is also important to consider chemical interactions with the perovskite. Some combinations may result in accelerated degradation, but the HTL may also protect the perovskite from external factors. [17]

A popular high-performance material for perovskite solar cells is the 2,2',7,7'-tetrakis(N,N-di-p-methoxyphenylamino)-9,9'-spirobifluorene (Spiro-OMeTAD), depicted in Figure 2.10. It was first used with perovskite in 2012 by Kim et al. to replace the liquid electrolyte used in prior cells, yielding a PCE of 9.7 % along with with increased device stability. [11, 28] Although Spiro-OMeTAD has been used to great effect, it presents several issues as well. First, its fabrication is complicated with several steps and bears a low yield, making Spiro-OMeTAD expensive, and a significant contributor to the total cost of a PSC. Adding even further to the price is the need for p-type dopants, which Spiro-OMeTAD requires in order to attain sufficient levels of conductivity and hole mobility. [29] Typical dopants are for example cobalt (Co(III)) -complexes and bis(trifluoromethane)sulfonimide lithium salt
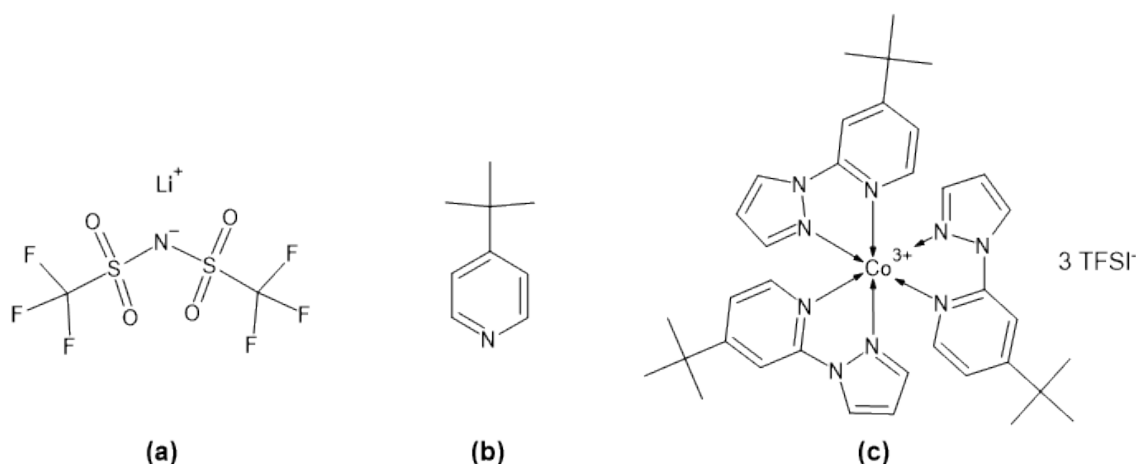
Figure 2.11. *Structural formulas of common dopants used with Spiro-OMeTAD: (a) Li-TFSI, (b) tBP, and (c) FK209.*

(Li-TFSI) in combination with the morphology improving 4-tertbutylpyridine (tBP) additive. [16, 30] The structural formulas of these dopants have been presented in Figure 2.11, with tris(2-(1H-pyrazol-1-yl)-4-tert-butylpyridine)cobalt(III)tris[bis(trifluoromethylsulfonyl)imide] (FK209) specifically shown here due to its use in this work. However, in addition to increased cost and complexity in fabrication, HTL doping may also contribute to solar cell instability. Namely, tBP has been reported to corrode the perovskite layer, while Li-TFSI elements can migrate through the doped Spiro-OMeTAD film under air exposure, creating pinholes in the process. [31, 32] Due to all these factors, the search for more cost-effective hole transport materials is constantly ongoing.

Other examples of common organic HTL materials are poly[bis(4-phenyl)(2,4,6-trimethyl-phenyl)amine] (PTAA) and poly(2,3-dihydrothieno-1,4-dioxin)-poly(styrenesulfonate) (PE-DOT:PSS) polymers, which have also seen use in inverted PSCs. They produce more uniform films, and PTAA has reached efficiencies over 20 %. PEDOT:PSS however suffers from significantly lower performance. Inorganic HTL materials on the other hand carry the advantage of greater stability in comparison to organic substances, possibly even acting as encapsulants for the perovskite. Noteworthy examples include copper gallium oxide ($CuGaO_2$) for n-i-p devices and nickel oxide (NiO_x) for p-i-n structured PSCs. Even though the addition of a HTL provides clear advantages, it is not a necessity for perovskite solar cells, as there have been successful designs without one. [33] Despite this, the highest performances have been achieved with a HTL, thus motivating their continued use.

3. MATERIALS AND METHODS

This chapter explains the experiments carried out in this thesis, which form its main core. First, the subject of this work, the fluorene-based hole transporting materials is introduced, followed by the substances and methods used in device fabrication. Finally, the methods of material and solar cell performance characterization are explained.

3.1 Fluorene-based hole transport materials

The hole transport materials studied in this thesis were designed and synthesized by Dr. Roberto Grisorio at Politechnico di Bari in Italy. They are all based on the same central fluorene structure, with different substituents. The structural formulas of the substances and their synthesis are presented in Figure 3.1 and their HOMO levels are presented in Table 3.1. A thorough electrochemical and thermal characterization of these substances has also already been carried out in Italy and will not be addressed in this work.

As can be seen from Figure 3.1, the synthesis of these HTMs is relatively simple and their estimated material cost is roughly 10 €/g, which is significantly lower than that of Spiro-OMeTAD at 77 €/g. [29, 34] Thus, these materials may provide a lower cost alternative to Spiro-OMeTAD, furthermore Spiro-OMeTAD requires dopants in order to reach its state-of-the-art performance. On the other hand, these new HTMs are adopted as dopant-free materials, with expected benefits on the device stability.

3.2 Solar cell manufacturing

The solar cells were made in the standard n-i-p structure following a protocol commonly used in the Hybrid Solar Cells team. The materials and techniques used in this fabrication process are discussed layer by layer in the following sub chapters 3.2.1-3.2.4, while figure 3.2a gives a simplified presentation of the solar cell structure. All materials were used as received unless stated otherwise.

Table 3.1. HOMO levels of the hole transport materials.

HTM	DC77	DC79	DC81	DC83
HOMO (eV)	-4.97	-5.03	-5.11	-5.24

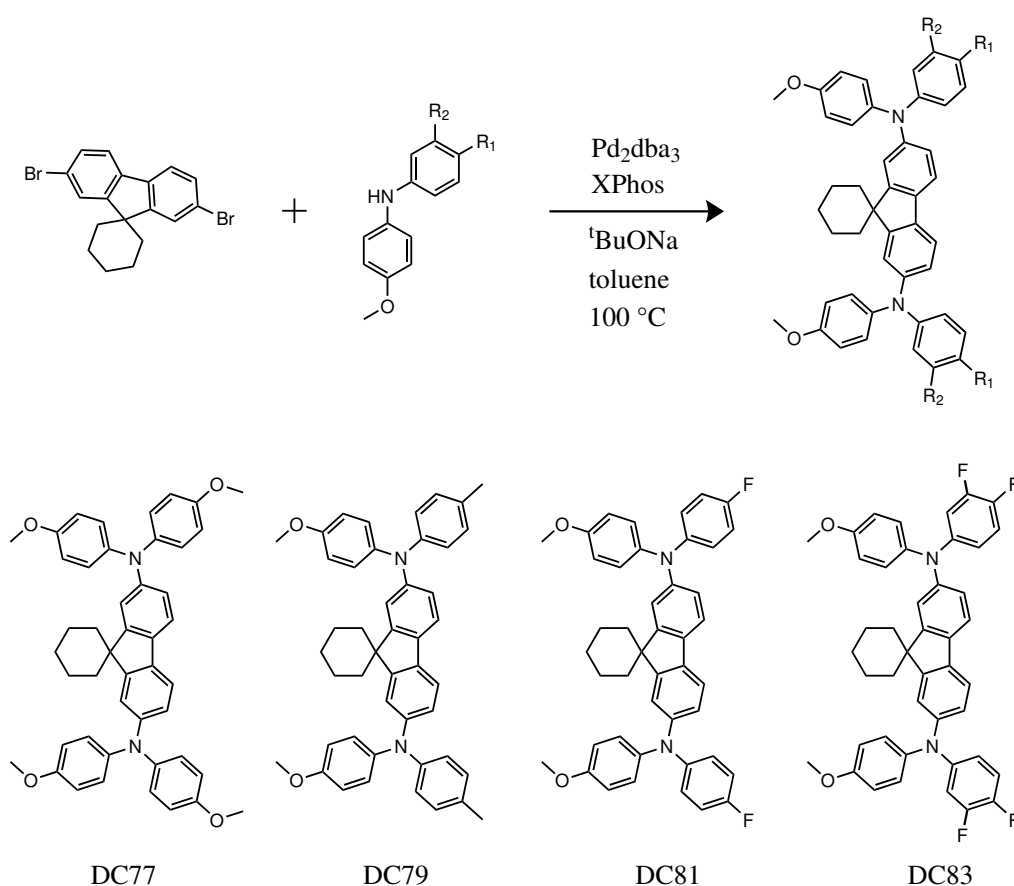*Figure 3.1.* The synthesis and structural formulas of fluorene-based hole transport materials studied in this work, labeled as DC77, DC79, DC81, and DC83.
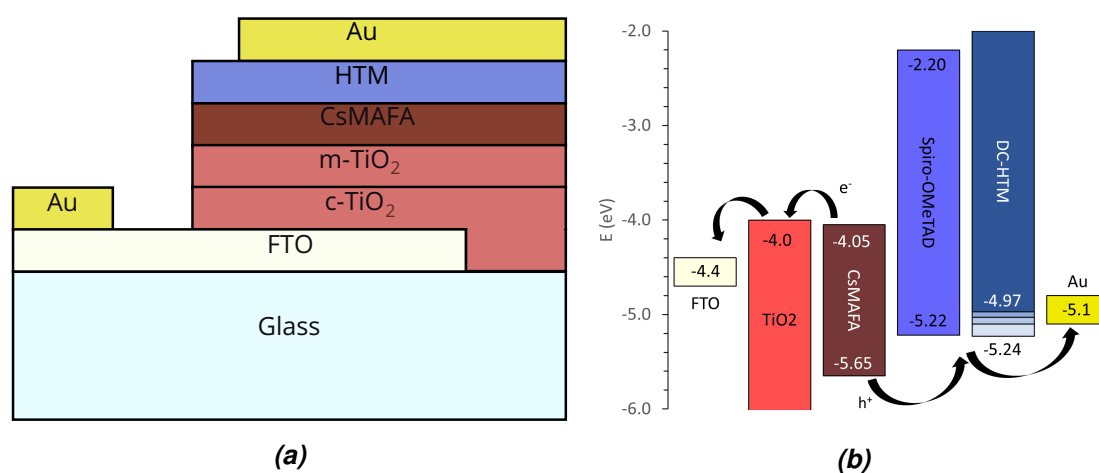

Figure 3.2. (a) A simplified cross-section and (b) schematic energy level diagram of the manufactured solar cells with doped Spiro-OMeTAD and DC-HTMs. The energy levels of materials other than the DC-HTMs were taken from literature. [35]

Figure 3.2b also presents a schematic energy level diagram of the manufactured solar cell constituents, with the values of materials other than DC-HTMs taken from literature. [35] Interestingly the HOMO levels of DC77 and DC79 are higher than the gold electrode, unlike Spiro-OMeTAD. However, it is worth emphasizing that the HOMO values are derived from electrochemical characterization in solution. Hence, the actual values of HTM films may deviate from from the electrochemical ones.

3.2.1 Substrate and electrodes

The solar cells were fabricated on glass substrates, that were precoated with the bottom electrode material, and for this purpose TEC 15 fluorine-doped tin oxide (FTO) glass with 2.2 mm thickness from Greatcell Solar was used. The substrate was first cut to 20 mm $\times$ 20 mm pieces, which were then chemically etched to remove the FTO layer from one side, as seen in figure 3.2a. The purpose of etching is to prevent short circuit during measurements and to more clearly determine the active area of the solar cell. To start with, the FTO was protected with Scotch 810 Magic tape so that a 4 mm strip was left uncovered. The bare FTO surface was then coated with zinc powder and 100 ml of 2.4 M hydrochloric acid solution was poured onto the substrates. After 5 minutes the etched area was gently brushed, and the substrates were rinsed with water to remove acid traces. After drying the resistance of the etched area was checked with a RS PRO IDM 72 handheld digital multi-meter to ensure it was above 0.8 MΩ.

Following etching, the substrates were first cleaned with a brush and 2 % Mucasol solution in water and rinsed with deionized water. After this, they were treated in ultrasonic bath sequentially for 15 minutes each in deionized water, acetone, and 2-propanol. Finally, the substrates were dried by blowing them with nitrogen, after which they were sealed in clean Petri dishes with parafilm.

Once all the other solar cell layers were finally deposited, the gold (Au) top electrode was evaporated through a mask via vacuum deposition. This method produces patterned thin films with good thickness control. The samples were placed in the vacuum deposition unit's (Edwards Auto 306) rotating sample holder, covered by a shadow mask. Small grains of Au, amounting to 400-500 mg were placed in a molybdenum "boat" below the samples. The chamber was then sealed and pumped to vacuum of approximately $5 \cdot 10^{-6}$ mbar. The material was evaporated by running an electric current through the boat, with the evaporation rate gradually increased up to 0.12 nm/s and kept constant until a thickness of 100 nm had been achieved.

The pattern produced by the mask can be seen in Figure 3.3. There are 3 cells on each substrate with active areas of 20 mm^2 with separate spots for connecting wires. The bottom electrode is also covered with the evaporated material to improve contact during measurements. This is also illustrated in Figure 3.2a.
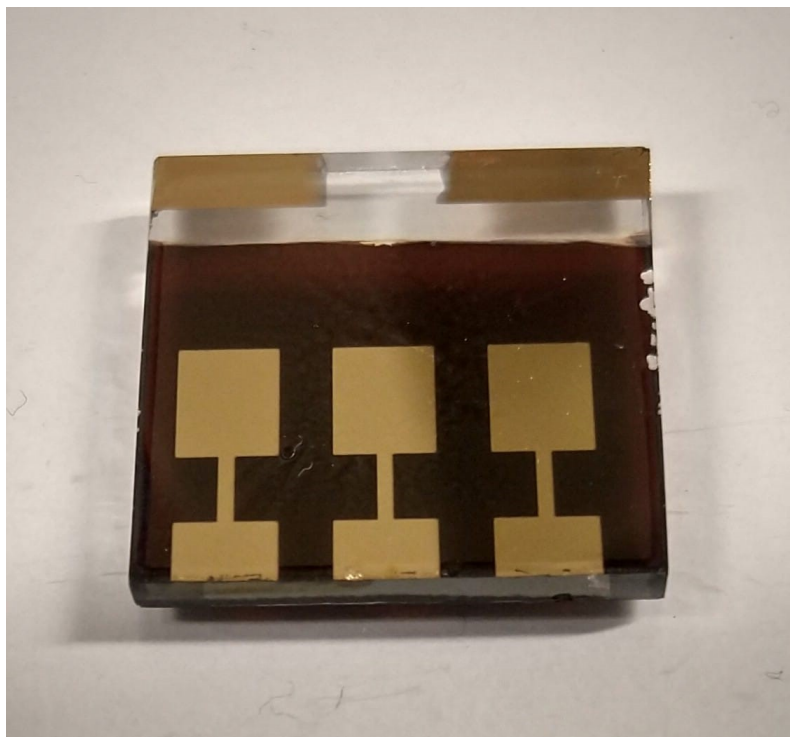
Figure 3.3. *An example of a standard n-i-p structure solar cell with DC81 as the HTM, demonstrating the pattern of the evaporation mask.*

3.2.2 Electron transport layer

These mesoporous n-i-p structure cells utilized a combination of both a compact and a mesoporous titanium dioxide (c-TiO$_2$ and m-TiO$_2$) as the electron transfer layer. First, the compact layer was deposited on the FTO via spray pyrolysis. The precursor solution was made from Sigma-Aldrich titanium diisopropoxide bis(acetylacetonate) stock solution (75 % in 2-propanol) by further diluting it to approximately 17.3 vol% with 2-propanol. The substrates were placed in an oven and covered with glass so that the side opposite to the etched area remained protected from the sprayed material. The oven was then heated to 450 °C and the substrates were coated by spraying 12 layers of the precursor solution with a spray gun using nitrogen as the carrier gas, with 20 seconds between each cycle. Afterwards the substrates were annealed at 450 °C for at least 45 minutes, before they were left to cool down.

The mesoporous layer on the other hand was deposited by spin coating. The solution was prepared from Greatcell Solar 30 NR-D TiO$_2$ paste, which was further diluted with ethanol (150 mg/ml). The solution was then stirred overnight until use. The FTO surface on the substrates that had been protected in the previous c-TiO2 step was then taped to prevent it once again from being covered over. 80 μl of the solution was then spin coated on the substrates at 4000 rpm for 10 seconds (acceleration of 2000 rpm/s). Substrates were then placed on a hotplate at 100 °C for a few minutes before sintering with the

Table 3.2. *The heating program used for sintering the mesoporous TiO$_2$ films.*

Ramp (min)	5	15	5	5
T ($^\circ$C)	125	325	375	450
Hold (min)	5	5	5	30

procedure presented in Table 3.2. After sintering, the substrates were removed from the oven at approximately 150 $^\circ$C and immediately moved into the nitrogen filled glovebox for the perovskite layer deposition.

3.2.3 Active layer

A hybrid organic-inorganic triple-cation Cs$_{0.05}$(MA$_{0.17}$FA$_{0.83}$)$_{0.95}$Pb(I$_{0.83}$Br$_{0.17}$)$_3$ (CsMAFA) perovskite was used as the photoactive layer for these experiments. It was deposited on the m-TiO$_2$ by spin coating a perovskite precursor solution. The following chemicals were used to prepare it:

- Dimethyl sulfoxide (DMSO), anhydrous 99.9 % Sigma-Aldrich
- *N,N*-Dimethylformamide (DMF), anhydrous 99.8 % Sigma-Aldrich and Alfa Aesar
- Cesium iodide (CsI), ultra dry 99.998 % abcr
- Formamidinium iodide (FAI), >99.99 % Greatcell Solar Materials
- Methylammonium bromide (MABr), >99.99 % Greatcell Solar Materials
- Lead(II) iodide (PbI$_2$), 99.99 % TCI
- Lead(II) bromide (PbI$_2$), >98.0 % TCI

First, a CsI stock solution in DMSO was prepared with a 1.5 M nominal concentration. The other solid substances were then scaled and mixed together to make a solution in DMSO/DMF (1:4 volume ratio). The nominal concentrations were FAI 0.95 M, MABr 0.19 M, PbI$_2$ 1.1 M and PbBr$_2$ 0.20 M. Once the solids had mostly dissolved, the CsI stock solution was added to the precursor solution in a 1:25 ratio. Finally, the completed solution was left in magnetic stirring for 24 to 48 hours before use.

The perovskite was deposited on the glass/FTO/c-TiO$_2$/m-TiO$_2$ substrate via a two-step spin coating program. First 50 μl of the perovskite solution was spread on the substrate and the spinning was swiftly started at 1000 rpm for 10 seconds with a ramp of 200 rpm/s, followed by the second step at 6000 rpm for 20 s, with a 2000 rpm/s ramp. 5 seconds prior to the end of the program 100 μl of chlorobenzene (99.8 % anhydrous, Sigma-Aldrich) was dispensed on the substrate to act as an antisolvent. After spinning, the substrate was immediately placed on a hotplate for annealing at 110 $^\circ$C for 60 minutes in order for the perovskite to crystallize properly.

3.2.4 Hole transport layer

The hole transport layer was spin coated on top of the perovskite film after it had cooled down from annealing. The solutions of the DC substances were simply prepared by dissolving typically 10 mg/ml of the substance in anhydrous chlorobenzene. The spiro-OMeTAD used as a reference was however more complicated as dopants were added to it. The materials used were:

- 2,2',7,7'-Tetrakis(N,N-di-p-methoxyphenylamino)-9,9'-spirobifluorene (Spiro-OMeTAD), >99.5 % Lumtec

- Chlorobenzene (CB), anhydrous 99.8 % Sigma-Aldrich

- 4-tert-butylpyridine (tBP), 96 % Sigma-Aldrich

- Bis(trifluoromethane)sulfonimide lithium salt (Li-TFSI), 99.95 % trace metals basis Sigma-Aldrich

- Tris(2-(1H-pyrazol-1-yl)-4-tert-butylpyridine)cobalt(III) tris[bis(trifluoromethylsulfonyl)imide] (FK209), >95 % Dyenamo

- Acetonitrile, anhydrous 99.8 % Sigma-Aldrich

First, Li-TFSI and FK209 were dissolved in separate solutions of acetonitrile with nominal concentrations of 1.8 M and 0.2 M respectively. These solutions could be used for up to 4 weeks. The doped Spiro-OMeTAD solution was then prepared by dissolving Spiro-OMeTAD in chlorobenzene to a 29.5 mmol/l concentration. The solution was heated at 60 °C for a few minutes to ensure Spiro-OMeTAD had completely dissolved. After the solution had cooled down tBP, Li-TFSI, and FK209 were added in 3.2, 0.53, and 0.1 molar equivalents to Spiro-OMeTAD respectively.

80 µl of the HTM solutions were deposited on the perovskite films by dynamic spin coating at 1800 rpm and the spinning lasted 30 seconds. Following film deposition, the substrates were left in a dry cabinet (10-15 % relative humidity) overnight before the gold electrodes were evaporated.

3.3 Characterization and performance testing

The new hole transport materials were tested using several methods, both to characterize the materials themselves and their performance in solar cells. These experiments have been divided into five subsections in this text: hole mobility and conductivity, photonic characterization, water contact angle measurement, cross-section imaging, and electric characterization.

3.3.1 Hole mobility and conductivity

Hole mobility is an integral property of a hole transport material as higher mobility means the holes can be more efficiently transferred through the hole transport layer. This property was tested using the *space-charge-limited current* (SCLC) method. The concept of space-charge considers electric charge to be distributed over a space, rather than as individual electrons or holes. It was first developed for vacuum diodes but was further expanded to semiconductors and insulators in a single-carrier device with the *Mott-Gurney law*. It states that for a thin slab of material with thickness d, the current density J is

$$J = \frac{9}{8}\epsilon_r\epsilon_0\mu_h\frac{V^2}{d^3} \tag{3.1}$$

where ϵ_r is the relative permittivity of the material, which is considered to be 3 for organic semiconductors, ϵ_0 is vacuum permittivity $8.854 \cdot 10^{-12}$ C V^{-1} m^{-1}, μ_h is hole mobility and V the applied voltage. The Mott-Gurney law assumes that the film is uniform without traps and the current is not primarily caused by doping of the material, which means that these factors would cause inaccuracies. [36]

For this experiment a special batch of hole-only samples with the structure glass/ITO/ PEDOT:PSS/HTM/MoO$_3$/Au was prepared. Aside from the DC-HTMs, samples with doped and undoped Spiro-OMeTAD were also prepared. The procedure for ITO, HTMs and Au was the same as with solar cell fabrication, whereas the PEDOT:PSS (Poly(3,4-ethylenedioxythiophene)-poly(styrenesulfonate), 1.3 wt% in H$_2$O, Sigma-Aldrich) and MoO$_3$ (molybdenum trioxide 99.97 % trace metals basis, Sigma-Aldrich) layers were slightly different. The PEDOT:PSS solution was mixed in 1:1 ratio with anhydrous DMF and 100 μl of the mixture was spin coated on the ITO substrate at 3000 rpm for 40 seconds, followed by annealing at 150 °C for 1 h. An approximately 3 nm thick layer of MoO$_3$ was evaporated on top of the HTM, in similar manner to Au.

The measurement itself was conducted using a computer-controlled Keithley 2450 Source Measure Unit (SMU) and measuring J-V curves between 0-2 V at a scan rate of 0.1 V s^{-1} in dark under ambient conditions. This data was then plotted in V^2, J-coordinates and a linear fit was applied to data points below 50 mA cm^{-2}. Hole mobility could then be calculated from the slope of the linear fit in accordance with formula 3.1.

Conductivity σ is also an important factor in charge transfer through these HTMs. It is the inverse of resistivity ρ and can thus can be calculated from the formula

$$\sigma = \frac{1}{\rho} = \frac{d}{RA} = \frac{d}{Rlt} \tag{3.2}$$

where d is the distance between measurement electrodes, R is the measured resistance and A is the cross-section area through which the current travels. For a thin film A
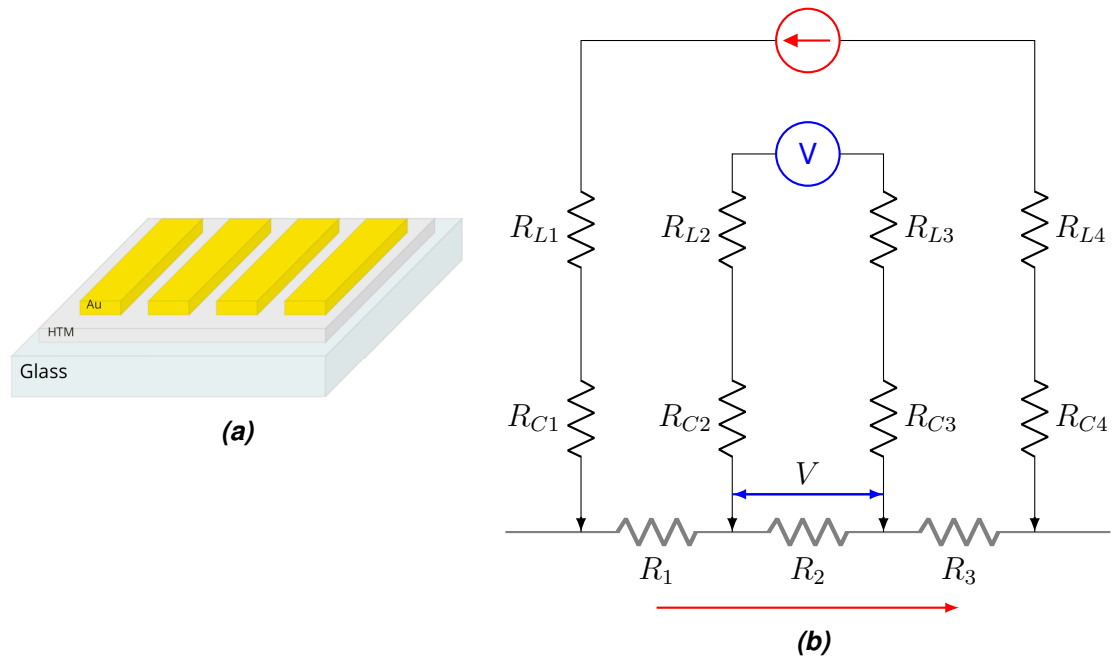
Figure 3.4. *(a) Simplified presentation of the samples used for conductivity testing. (b) A schematic of a four point resistance measurement, with lead resistances R_L and contact resistances R_C. The red arrow represents current flow.*

can then be calculated as the product of film thickness t and length of electrode l. [37] Figure 3.4a illustrates the samples used for this measurement. The glass substrates were cleaned following the same protocol as with FTO substrates, except that before deposition the substrates were treated for 1 minute in a PDC-002 Expanded Plasma Cleaner with a PlasmaFlo gas mixer (Harrick Plasma, USA) to improve surface wettability. The DC-HTMs and undoped Spiro-OMeTAD were soon spin coated to form approximately 100 nm thick films. The Spiro-OMeTAD film was prepared using the same protocol as for the solar cells, just without the dopants, whereas the DC-HTM solutions were made with the concentration of 30 mg/ml in CB and spin coated at 1400 rpm for 30 seconds. The film thicknesses were initially measured using a *contact profilometer* and further adjusted by optical UV-VIS absorption characterization prior to sample preparation.

Following HTM film deposition, the 100 nm Au electrodes were vacuum evaporated. A specially designed mask was used for this to deposit three sets of four electrodes on each substrate with $l =$22 mm and $d =$0.1 mm. Four electrodes were used in order to perform a *four-point resistance measurement*, which eliminates factors such as contact and lead resistance (R_C and R_L, respectively) that would affect the results. A schematic of the four-point measurement is presented in Figure 3.4b. The Keithley 2450 SMU was used to source current through the outer electrodes and the voltage drop V between the inner electrodes was then measured at different currents. The measured values were plotted in I, V-coordinates, and the resistance was obtained from the slope of a linear fit. The conductivities were then calculated using equation 3.2.

3.3.2 Optical and photophysics properties

Basic UV-VIS absorption spectra measurements were carried out for DC films spin coated on glass in the range 250-800 nm using a Shimazdu UV-1900i UV-VIS spectrophotometer.

Aside from absorption, the HTMs were also characterized using *photoluminescence* (PL) spectroscopy and *time-resolved photoluminescence* (TRPL) spectroscopy. In photoluminescence, a material is excited by a photon, which creates an electron-hole pair. This is then followed by relaxation of the system and *radiative recombination* of the electron-hole pair, which results in the emission of a photon of lower energy, and thus, longer wavelength than the original. The excitation energy was kept constant during the measurements, while the detection energy was varied to detect the photons emitted from the sample. [38]

In a solar cell, there would ideally be no radiative recombination, as the charges would be separated towards their respective electrodes. Therefore, the amount of quenching caused by a HTM in a PL measurement compared to bare perovskite can serve as an indication of the efficiency of hole extraction in the CsMAFA/HTM interface. For these measurements, samples with the structure glass/CsMAFA and glass/CsMAFA/HTM with all the DC substances and doped Spiro-OMeTAD were prepared by spin coating using the same procedures as in solar cell fabrication, except that the glass substrates were plasma cleaned prior to HTM deposition to improve the wettability of the surface and ensure proper spreading of the perovskite. The steady-state PL spectra were measured with a FLS1000 spectrofluorometer (Edinburgh Instruments, UK), excited at 600 nm.

TRPL measurement observes the photoluminescence intensity as a function of time, providing information about the decay of the excited state. More specifically, time-correlated single photon counting (TCSPC) was used. It uses a short laser pulse to excite the observed material and the first emitted photon is recorded with the delay between photon arrival and excitation laser pulse measured. This process is quickly repeated to construct a histogram of the number of photons counted at a specific time. TCSPC is a statistical method and it provides very good information about the intensity dynamics of the sample. [39] The decays were measured with a TCSPC apparatus equipped with a Picoharp 300 controller and a PDL 800-B driver for excitation and a Hamamatsu R3809U-50 microchannel plate photomultiplier for detection in 90° configuration. The samples were excited at 405 nm with a time resolution of 60 ps and the photons were detected at 755 nm.

3.3.3 Water contact angle

In the conventional structure, the hole transport layer is on top of the solar cell and thus protects the perovskite layer, which is vulnerable to environmental factors, especially moisture. Thus, the *hydrophobicity* of the HTM is of interest and this property can be

tested by measuring the water contact angle (CA). CA is the angle between the examined surface and the tangent of a liquid's surface, in this case the HTM film and water droplet respectively. The CA is affected by several factors, but for the purposes of this thesis comparing the angles of the samples is sufficient. Typically water CA greater than 90° is considered to be hydrophobic with smaller angles indicating a *hydrophilic* material. [40] These measurements were taken from the same samples as PL and TRPL by using an Attension Theta Lite optical goniometer (Biolin Scientific AB, Sweden).

3.3.4   Scanning electron microscopy imaging

Scanning electron microscopy (SEM) is a versatile technique that uses a focused electron beam to irradiate an area or volume of a material. Interaction with the electron beam produces signals in the form of for example secondary and backscattered electrons, characteristic x-rays, and photons of varying wavelength. These signals can be used to analyze many properties of the sample such as surface topography or composition. [41] Particularly, in this work SEM was used to image cross-sections of the fabricated solar cells.

3.3.5   Electric characterization

Several batches of solar cells were manufactured over the span of four months first to optimize their performance and then to verify the reproducibility of the results. The J-V curves of these solar cells were recorded using the same Keithley 2450 SMU and a SS150-AAA solar simulator (Sciencetech, Canada) with a 150 W Xenon lamp and AM1.5G filter. The measurement was calibrated to 1 sun, or 100 mW/cm^2 using a KG5 calibrated reference cell and meter (Newport, USA). Measurements were also performed in darkness. The scans were performed in the range of -0.2 to 1.2 V, in reverse and forward direction at a scanning rate of 0.05 V s^{-1}. Unfortunately, the solar simulator broke down partway through, but a neighbouring research team's TriSOL class AAA solar simulator (OAI, USA) could be borrowed to carry on the experiments. The primary difference however was that said simulator did not have an AM1.5G filter so another filter had to be used instead. In testing it was found that out of the available choices, an AM0 filter was most comparable to the earlier measurements. This means that the results obtained from these measurements are not perfectly comparable, but that data is still presented in this thesis, and the used filter is specified.

The main parameters observed in these measurements were PCE, J_{SC}, V_{OC} and FF. Series and shunt resistances (R_S, R_P) of the cells were also derived from the J-V curves. Most cells were measured the day after the fabrication was completed and again a week later, as this duration proved to induce a great difference. The long-term stability of the

Table 3.3. *Batches of produced solar cells, their purpose and the time over which they were monitored.*

Batch	Experiment	Measurement period
1	First attempt, 10 mg/ml DC concentration	106 days
2	DC77 concentration testing	1 week
3	Dopant testing on DC77, DC79	1 week
4	DC79 concentration testing	1 day
5	Standard 10 mg/ml batch	once after 6 days
6	Standard 10 mg/ml batch	1 week
7	Standard 10 mg/ml batch	1 week

first successful batch of cells was also monitored. All cells were initially stored in a dry box, with a relative humidity of 10-15 %, while the half of the stability samples were kept in ambient air (relative humidity 40-50 %) following the first measurement. In both cases the temperature was 20 °C. The batches and their purpose are listed in Table 3.3.

A commonly employed concentration of 10 mg/ml was chosen to start the experiments. In batches 2 and 4 concentrations of 5, 15 and 20 mg/ml were tested with DC77 and DC79 respectively. On the other hand, batch 3 was used to test doped DC77 and DC79. The same dopants were used as with Spiro-OMeTAD, in the same concentrations.

The quantum efficiencies of the cells were also examined using the Newport QuantX-300 Quantum Efficiency Measurement Solution. This device allowed the measurement of both internal and external quantum efficiency at specific wavelengths of light. The measurements were performed between 300-800 nm for one each of the DC-HTMs solar cells and a reference Spiro-OMeTAD cell.

4. RESULTS AND DISCUSSION

This chapter discusses the results obtained from the experiments, starting with the characterization of the DC-HTMs themselves in section 4.1, before moving on to the information obtained from the characterization of the fabricated solar cells in sections 4.2 (performance) and 4.3 (stability).

4.1 Characterization

4.1.1 Hole mobility and conductivity

Looking at the current density-voltage (J-V) curves for hole mobility (μ_h) determination by SCLC measurement (see Section 3.3.1) depicted in Figure 4.1, it would at first seem that the hole mobilities of the DC substances are close to that of doped Spiro-OMeTAD. However, the spin coated DC layers were significantly thinner (90 nm) than Spiro-OMeTAD film (180 nm). This results in hole mobilities that are in a similar order of magnitude as undoped Spiro-OMeTAD. This can be seen in Table 4.1, which presents the average hole mobilities of the HTMs gained from the characterization of 3 samples. The derived hole mobilities of doped and undoped Spiro-MeTAD correspond quite well with reported values [42, 43]. There is a rather clear difference between the DC-HTMs, with DC77 having the highest μ_h, DC79 slightly lower, and DC81 and DC83 having similarly lowest values.

The conductivities (σ) of these HTMs were also determined (see Section 3.3.1) and the data is presented in Table 4.1. Doped Spiro-OMeTAD could unfortunately not be mea-

Table 4.1. *Average hole mobilities μ_h (cm^2 V^{-1} s^{-1}), and conductivities σ (S cm^{-1}) of the HTMs. The conductivity of doped Spiro-OMeTAD could not be measured.*

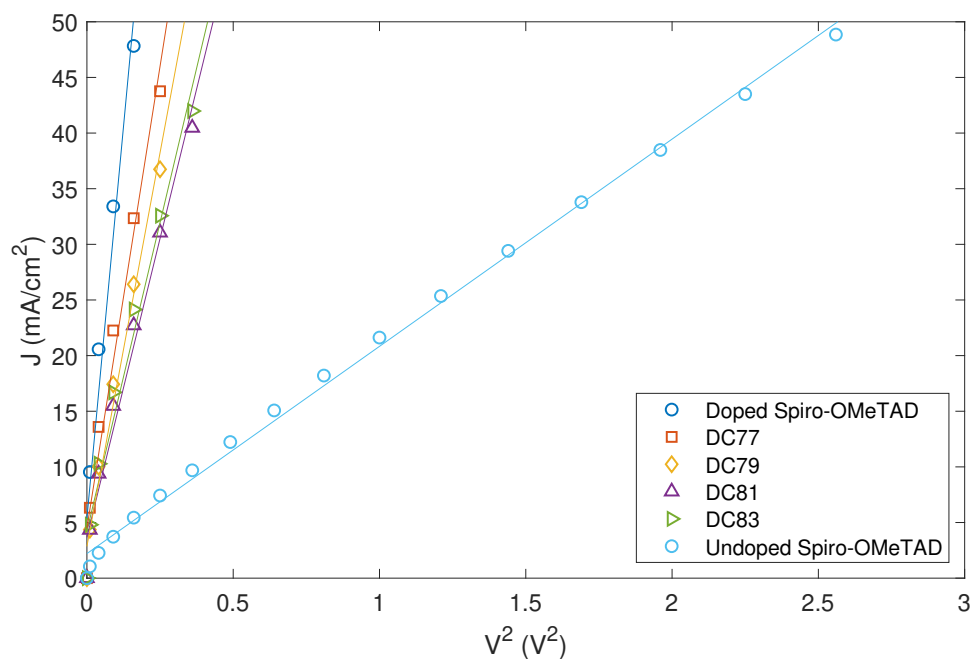| HTM	μ_h (10^{-5} cm^2 V^{-1} s^{-1})	σ (S cm^{-1})
Undoped Spiro-OMeTAD	4.2±0.4	$9.6 \cdot 10^{-8}$
Doped Spiro-OMeTAD	49.3±6.8	–
DC77	5.7±1.2	$1.5 \cdot 10^{-6}$
DC79	3.6±0.6	$5.7 \cdot 10^{-7}$
DC81	2.2±0.3	$4.6 \cdot 10^{-7}$
DC83	2.2±0.3	$2.1 \cdot 10^{-7}$

Figure 4.1. *A set of SCLC measurements, limited to the area unto which linear fits were performed in order to calculate hole mobilities using equation 3.1.*

sured as a smooth film could not be formed on a glass substrate, so undoped Spiro-OmeTAD served as a reference for this measurement. This has been reported to have values of σ ranging from $3 \cdot 10^{-8}$ to $1.3 \cdot 10^{-7}\,\mathrm{S\,cm^{-1}}$, with one article in particular presenting $9.0 \cdot 10^{-8}\,\mathrm{S\,cm^{-1}}$. [42, 44, 45] This means that our result could be considered fairly reliable. All DC-HTMs displayed greater values of conductivity, in a rising order from DC83 to DC77. However, they are significantly lower than what has been reported for doped Spiro-OMeTAD, with a conductivity up to the $10^{-5}-10^{-4}\,\mathrm{S\,cm^{-1}}$ range. [37, 42, 46]

A HTM with low hole mobility and conductivity naturally leads to lower solar cell performance, especially if the HTM film is thick. Thus, dopants may be necessary for these HTM substances to perform at a comparable level to doped Spiro-OMeTAD.

4.1.2 Optical and photophysical properties

The normalized UV-VIS absorption spectra of the DC-HTM films, alongside that of undoped Spiro-OMeTAD reference are depicted in Figure 4.2a. The DC-HTMs exhibit absorption peaks at roughly similar wavelengths as Spiro-OMeTAD, which implies they should have fairly similar optical band gaps.

On the other hand, the PL and TRPL measurements yielded promising results for some of the DC substances. The measured PL spectra can be seen in Figure 4.2b. The quenching efficiencies, i.e. hole extraction yields of the HTMs, were estimated from these results and are presented in Table 4.2. These results show that DC77 has comparable
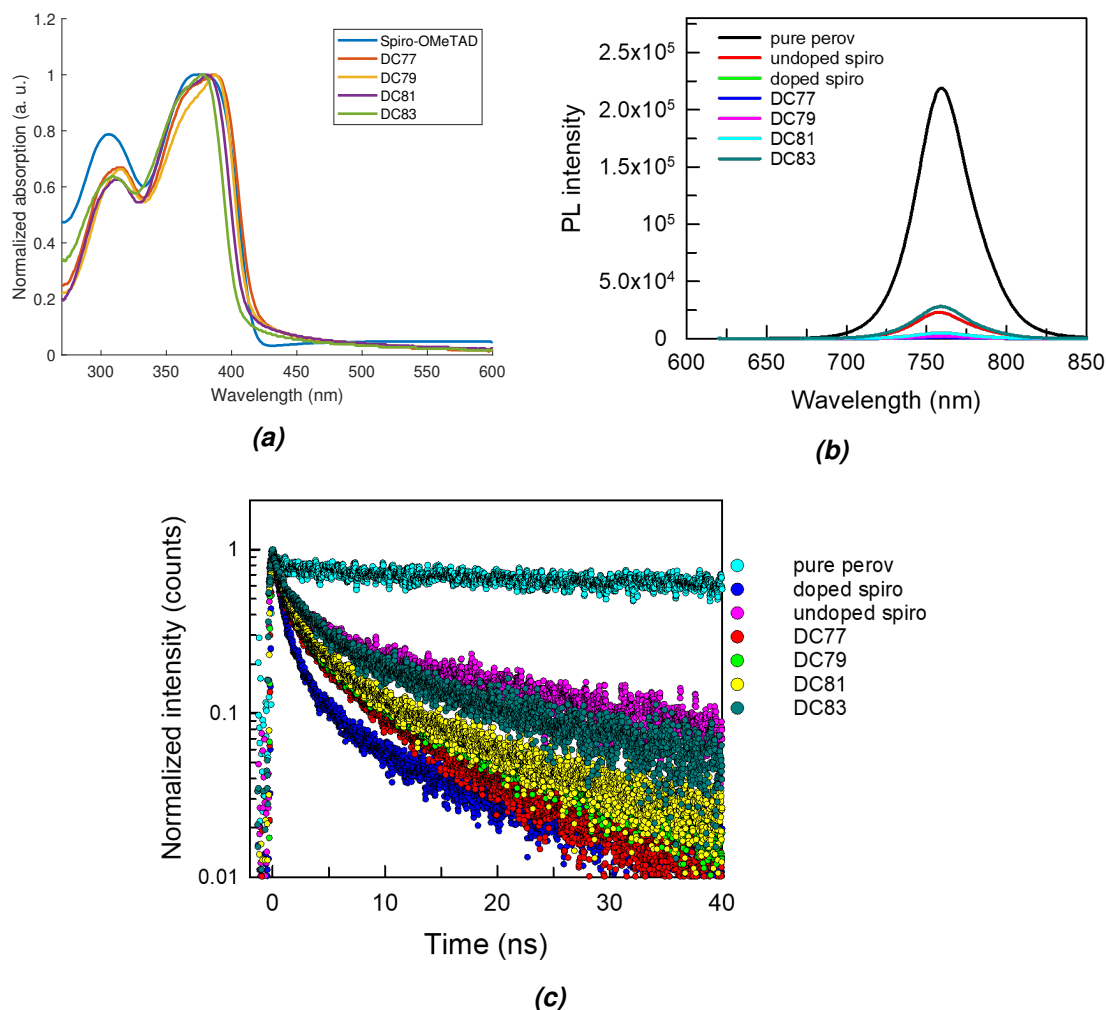
Figure 4.2. *(a) Normalized absorbance spectra of glass/HTM films with undoped Spiro-OMeTAD for refence. (b) Photoluminescence (PL) spectra and (c) time-resolved PL (TRPL) decays of glass/CsFAMA and glass/CsFAMA/HTM films with the DC-HTMs and both doped and undoped Spiro-OMeTAD.*

ability to extract holes from the perovskite layer in comparison to doped Spiro-OMeTAD, with the other DC substances offering in turn decreasing quenching efficiency, and DC83 performing close to undoped Spiro-OMeTAD. This implies that the HOMO levels of DC-HTMs (apart from DC83) are well aligned with the valence band of CsMAFA perovskite. This also correlates quite well with the HOMO levels presented in Table 3.1, with DC83 clearly having the lowest HOMO.

The time-resolved PL decays are presented in Figure 4.2c. They further reinforce the results obtained from the PL spectra, with doped Spiro-OMeTAD having the fastest decay and the DC-HTMs decay accelerating in order from DC83 to DC77, with the decay rate serving as an indicator of the charge extraction speed. Considering all these results, DC77 and DC79 seem to form a quite favourable interface with CsMAFA perovskite, despite having fairly low hole mobility and conductivity. This could make them still useful in

Table 4.2. *Quenching efficiencies, i.e. hole extraction yeilds, of the studied HTMs esti-mated from the PL measurements.*

HTM	Quenching (%)
Undoped Spiro-OMeTAD	89.8
Doped Spiro-OMeTAD	99.6
DC77	99.7
DC79	99.1
DC81	97.8
DC83	87.5

(a) DC77   *(b) DC79*   *(c) DC81*

(d) DC83   *(e) Undoped Spiro-OMeTAD*   *(f) Doped Spiro-OMeTAD*
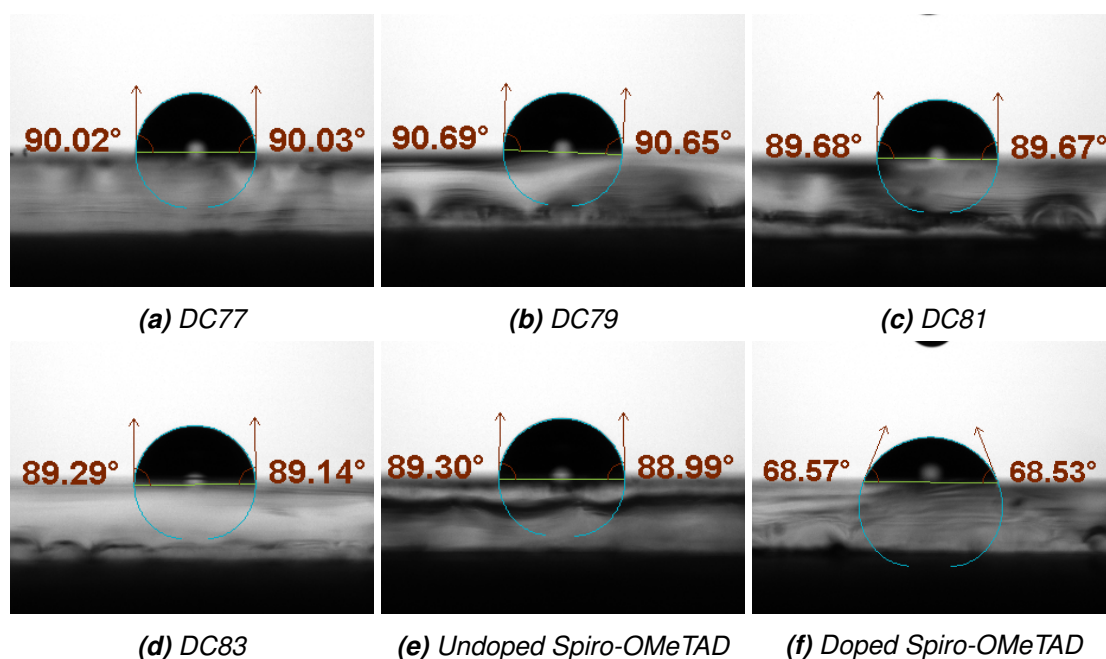
Figure 4.3. *Images from the water contact angle measurement of different HTMs. The angles are marked in each image.*

applications where a thin hole transporting layer is preferred, such as in p-i-n structure solar cells, as a thick layer could block light from reaching the active layer.

4.1.3 Water contact angle

The results from water contact angle (CA) measurement clearly show that the DC sub-stances form a more hydrophobic film than doped Spiro-OMeTAD, while undoped Spiro-OMeTAD had a CA in the same range as DC81 and DC83. Li-TFSI and tPB are hygro-scopic and doping Spiro-OMeTAD with them has been shown to make more hydrophilic films and thus this result was not surprising. [47, 48] Both DC77 and DC79 have con-tact angles barely above 90° and thus could be considered hydrophobic. These contact angles seem favourable for the long-term stability of the DC solar cells.
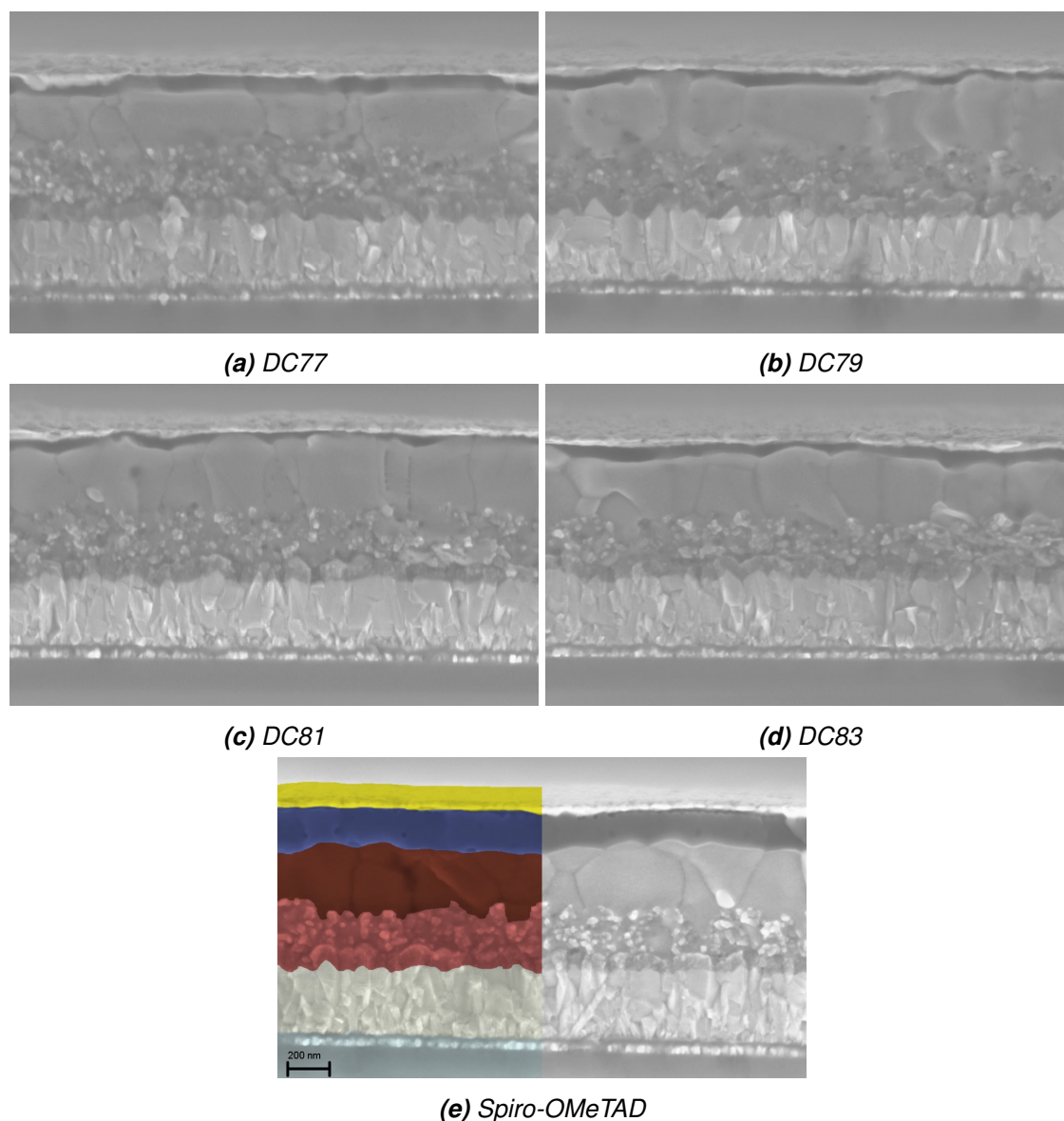
(a) *DC77*

(b) *DC79*

(c) *DC81*

(d) *DC83*

(e) *Spiro-OMeTAD*

Figure 4.4. *SEM cross-section images of the fabricated solar cells. Reference Spiro-OMeTAD cell has been coloured to match the layers in figure 3.2a and the scale bar is the same in all images.*

4.1.4 Cross-section imaging

Figure 4.4 presents examples of SEM cross-section images of the fabricated solar cells. It is immediately clear from these images, that the primary difference between the cells with DC-HTMs and Spiro-OMeTAD is the thickness of the hole transport layer. Spiro-OMeTAD is approximately 150 nm thick, whereas the thickness of DC-HTMs ranges from 90 nm to the perovskite layer practically touching the Au electrode. It was expected that the DC hole transport layers would be thinner due to the lower concentration of their solutions, but it was assumed that the film would have mostly uniform thickness. It may be that the wetting properties of the DC-HTM solutions are not perfectly favourable on the perovskite.

Table 4.3. *Average performance of solar cells prepared with different concentrations (ρ_i) of DC77 and DC79.*

HTM	ρ_i (mg ml^{-1})	PCE (%)	FF (%)	J_{SC} (mA cm^{-2})	V_{OC} (V)
DC77	10	8.9	43.3	21.7	0.95
	20	7.3	32.8	22.1	1.01
DC79	5	4.0	38.0	16.2	0.65
	10	7.9	38.6	20.4	1.00
	15	5.5	26.0	20.6	1.03
	20	2.5	15.9	15.9	0.99

It is also worth noting that the cells have quite thick electron transport layers, with the c-TiO$_2$ and m-TiO$_2$ averaging roughly 70 and 240 nm, respectively. These layers are reported in literature with thicknesses in the 20-30 and 100-150 nm range, which means their thickness may in fact hinder electron transportation. Also, the pure perovskite layer is in turn thinner instead of the reported 400-500 nm, although it does mix with the m-TiO$_2$ layer, as seen in Figure 4.4. [49]

4.2 Solar cell performance

As stated earlier in section 3.3.5, the starting concentration of 10 mg/ml for DC spin coating solution was used for most of the devices, as it produced the best results of all tested concentrations. The average parameters of the tested devices in batches 2 and 4 are presented in Table 4.3. With DC79 we clearly observe that significantly deviating from 10 mg/ml reduces device performance. More concentrations were unfortunately not tested with DC77 due to an accident in manufacturing, but a reduced performance was also observed at higher concentration. This difference became even clearer after one week, when the average PCEs were 11.2 % and 8.5 % for 10 and 20 mg/ml respectively. The low conductivity and hole mobility may explain why higher concentrations resulted in decreased performance, as they affect the fill factor of the cell. The poor V_{OC} with 5 mg/ml on the other hand could stem from the HTL being practically nonexistent as SEM images already proved the HTL to quite thin at 10 mg/ml.

The concentration testing did not cover DC81 and DC83 due to their lower performance at 10 mg/ml that placed less expectations for them. Thus, it was just assumed that the same concentration would also work for them as it did with DC77 and DC79. Therefore, all further solar cells were made with the same concentration. The PCEs of all devices fabricated with 10 mg/ml and doped Spiro-OMeTAD references are presented in Figure 4.5, both a day after Au electrode evaporation, and after approximately one week. Table 4.4 further details average parameters obtained from these solar cells.
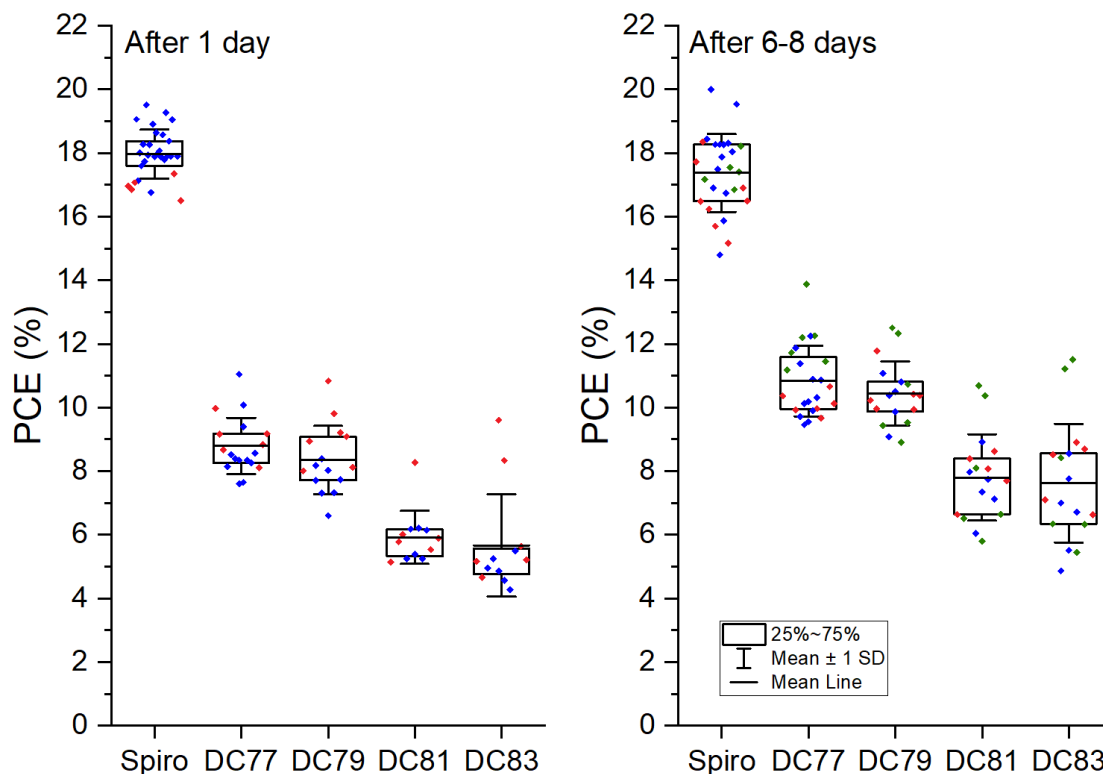
Figure 4.5. *The power conversion efficiencies of manufactured standard n-i-p struc-*
ture solar cells, measured one day after electrode evaporation and again approximately
a week later. Blue dots present measurements with AM 1.5G filter, whereas red and
green (batch 5) dots were measured with AM 0. All measurements were set to 1 sun
(100 mW cm^{-2}) according to a KG5 filtered Newport reference solar cell.

An interesting property of the solar cells made with the DC-HTMs becomes apparent
while looking at the collected results: their performance increases significantly after the
first measurement. It has been reported that exposure to ambient air can improve the
conductivity of Li-TFSI doped Spiro-OMeTAD over several hours, but it was not expected
that the undoped DC solar cells would keep improving over the span of several days even
without doping. [50] For this reason, the cells were monitored for a week, and the later
results are considered the actual performance of these devices. While an improvement is
certainly a favourable outcome, these experiments did not explore the mechanism behind
this enhancement, which would require further study.

Another important factor to address regarding the results is the two different solar simula-
tors and filters used for the measurements. The values obtained are mostly comparable
between both, apart from a few cells measured with AM 0 filter for each DC substance
being clearly higher than others. For day 1 measurements it could be assumed that the
enhancement for these outstanding points was simply faster, as their PCEs are in a sim-
ilar range than those obtained on later measurements. There is, however, an explanation
for the highest points after 1 week. They all belonged to batch 5 (marked green in Figure

Table 4.4. *Mean values of solar cell parameters from all doped Spiro-OMeTAD reference and DC 10 mg/ml samples measured with both AM 1.5G and AM 0 filters. The active area of the cells was 0.2 cm^2. The values in brackets are from champion cells.*

(a) Measured after one day.

HTM	PCE (%)	FF (%)	J_{SC} (mA cm^{-2})	V_{OC} (V)
Spiro-OMeTAD	18.0±0.9	69.5±1.6	22.7±0.6	1.14±0.03
DC77	8.8±0.9	44.1±3.1	21.6±0.4	0.92±0.04
DC79	8.4±1.0	42.0±3.5	20.8±0.6	0.95±0.06
DC81	5.9±0.8	36.1±3.3	19.0±1.3	0.86±0.05
DC83	5.7±1.5	37.0±5.3	18.5±2.1	0.82±0.09

(b) Measured after one week.

HTM	PCE (%)	FF (%)	J_{SC} (mA cm^{-2})	V_{OC} (V)	R_S (Ω cm^2)[i]	R_P (kΩ cm^2)[i]
Spiro-OMeTAD	17.4±1.2 (20.00)	67.9±2.8 (72.22)	22.6±0.6 (23.47)	1.1±0.03 (1.18)	4.9	1.89
DC77	10.8±1.1 (13.87)	52.5±2.2 (57.24)	21.1±0.9 (23.30)	1.0±0.04 (1.04)	9.4	0.61
DC79	10.4±1.0 (12.68)	50.5±2.7 (53.19)	21.0±0.8 (22.49)	1.0±0.04 (1.06)	11.2	0.44
DC81	7.8±1.3 (10.69)	44.3±3.5 (46.27)	19.1±1.5 (22.21)	0.9±0.06 (1.04)	15.7	0.36
DC83	7.6±1.8 (11.51)	44.1±4.1 (52.80)	18.7±1.7 (21.37)	0.9±0.06 (1.02)	11.8	0.39

[i] Resistance values were calculated from the champion cells under 100 mW cm^{-2} illumination.

4.5) which was first measured 6 days after fabrication. They remained undisturbed for this period, which seems to have enhanced their performance to a greater extent. Therefore, the different solar simulator and filter did not have a clearly noticeable effect on the results.

As for the actual parameters of the solar cells, there are two distinct trends between the DC-HTMs: devices employing DC77 have the best performance with DC79 falling slightly behind, while DC81 and DC83 based devices have lower average parameters, as seen in Table 4.4b. However, all of them performed worse than doped Spiro-OMeTAD-cells, with the clearest difference observed in FF and PCE. There is also quite a clear difference in the series and shunt resistances obtained from the champion cells. According to Equation 2.4 the current generated by the cell reaches its maximum when $R_S = 0$ and $R_P \longrightarrow \infty$, meaning that the device based on Spiro-OMeTAD having the smallest R_S and largest R_P makes it the best out of the measured cells. This also correlates with an increased fill factor. [9] Once again, DC77 performs the best out of DC-HTMs in this regard as well. These results seem reasonable as they mostly align with the other parameters obtained from the champion cells, especially considering that the DC81 champion cell had the lowest fill factor, along with the worst resistance values. The J-V curves of the champion cells are presented in Figure 4.6a.

Figure 4.6b on the other hand shows an example of the external quantum efficiencies measured from the fabricated solar cells. All DC-cells have lower EQEs than with Spiro-
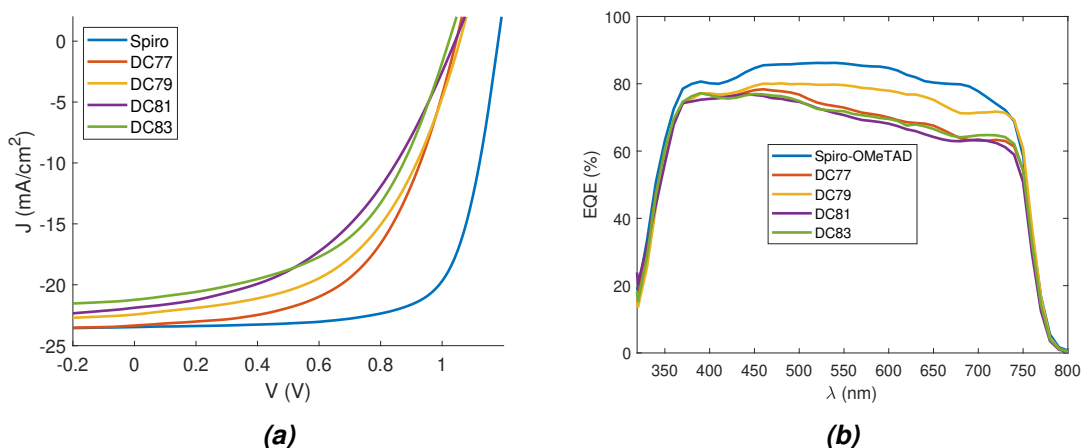
Figure 4.6. *(a) J-V-curves of the champion cells for each substance and (b) EQEs of solar cells fabricated with all the DC-HTMs and Spiro-OMeTAD for reference.*

Table 4.5. *Average parameters obtained from doped DC77 and DC79 solar cells, measured 1 week from fabrication. Champion device values have been marked in parenthesis.*

HTM	PCE (%)	FF (%)	J_{SC} (mA cm^{-2})	V_{OC} (V)
DC77	12.1±0.3 (12.41)	55.0±0.9 (55.99)	22.0±0.7 (22.17)	1.00 (1.00)
DC79	11.8±1.2 (13.43)	55.8±1.1 (57.30)	20.1±1.6 (21.90)	1.05±0.01 (1.07)

OMeTAD, however it is interesting to note that the DC79 device has the same general shape of the curve, resulting in higher EQE. The highest EQE should naturally also result in the highest PCE, which was not the case. This could be due to the EQE being measured from a small spot of the cell, which may have been superior for the DC79 cell. The other DC-HTM curves are sloped downwards at the higher wavelengths, which means that lower energy photons are being converted at a lesser efficiency.

Finally, let us address batch 3, made for the purpose of a brief doping test using the same dopants as with Spiro-OMeTAD. Comparing the results in Tables 4.5 and 4.4b an improvement can be seen in the average values, although the best doped DC77 cell still performs worse than the undoped DC77 champion, which also has similar performance to the doped DC79 cell. Considering the possible increase in hydrophilicity that these dopants may cause and the increased complexity, the improvement certainly does not seem overall beneficial. However, the fact remains, that the hole mobility of these DC-HTMs was rather poor and thus further study into doping them may be warranted. Different dopant concentrations and different dopants altogether would certainly be worth investigating.
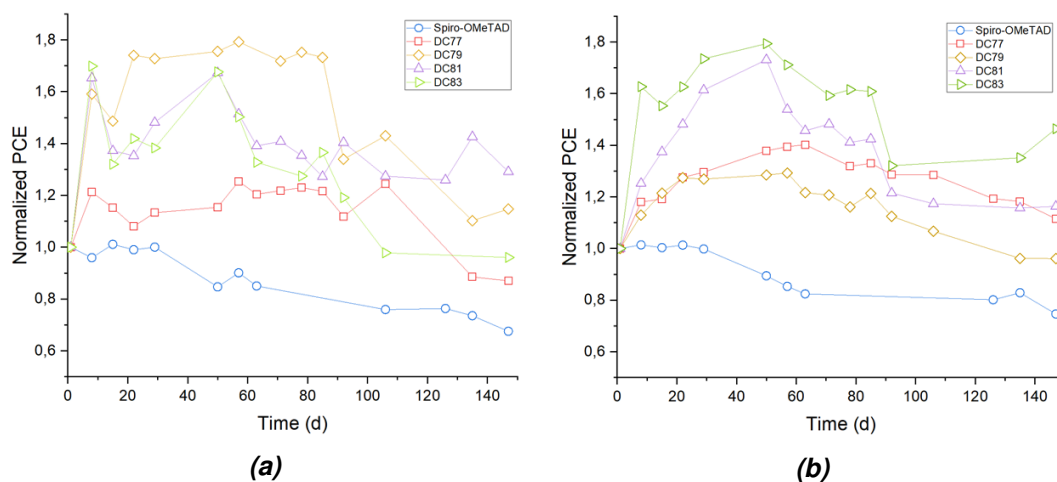
Figure 4.7. *Normalized PCEs of the solar cells from batch 1 stored in (a) ambient air and (b) dry cabinet with 10-15 % relative humidity over the observation period.*

4.3 Solar cell stability

Five samples from the first successful batch were stored in ambient air at the temperature of 20 °C and five in a dry cabinet at 10-15 % relative humidity, for the purpose of observing their degradation. The normalized power conversion efficiencies of these cells over time are presented in Figures 4.7a and 4.7b, respectively. While Spiro-OMeTAD cells simply declined over time, the PCE of devices employing DC-HTMs greatly improved (up to 80 % at peak) after the first measurement, as stated earlier. This magnitude of increase varies even between cells made with same HTM, as some cells were already more efficient at the time of the first measurement. All of the DC-HTM devices hit their peaks at around 50-70 days and start dropping off towards the end of the observation period. Compared to the Spiro-OMeTAD references, the longevity of these cells does indeed look favourable, as only DC77 and DC83 of the air-stored and DC79 of the dry box samples have decreased their PCE below their initial values. Even so, the rate of degradation following the period of improvement has been quite similar or even faster than Spiro-OMeTAD for most samples. Longer observation may result in the DC-HTMs falling below Spiro-OMeTAD.

Comparing the different storage conditions, samples stored in ambient air had a more distinct initial spike of improvement, while samples in the reduced humidity of the dry cabinet (except DC83) experienced a more gradual enhancement. It could be that water is somehow connected to the mechanism behind this improvement. Dry cabinet cells also seem to produce more consistent results, while there is more fluctuation between consecutive measurements with air-stored samples. This behaviour in turn may have to do with variation in the humidity of the ambient air. Regardless, the sample size is very small, making it meaningless to draw any greater conclusions from these comparisons. Even though the observation of a larger number of cells would have indeed provided more

Table 4.6. *An example from a DC81 sample of the rapid degradation following measurement. The three cells on the same substrate were measured one at a time and next week in reverse order.*

Time (d)	1 ↓	7 ↑
PCE_1 (%)	8.27	8.66
PCE_2 (%)	5.14	8.45
PCE_3 (%)	5.89	9.68

conclusive stability results, it was not possible due to time constraints.

The three week gap in measurements between days 29 and 50 was caused by the change in solar simulator. After 106 days, the solar simulator was switched back to the original with the AM 1.5G filter. This change does not seem to have significantly influenced the results as values of DC77 and DC79 based cells follow a fairly consistent trend throughout the experiment. The 3 weeks did however result in a large increase in PCE for DC81 and DC83 samples that were stored in ambient air. This however seems to be more a characteristic of these HTMs themselves, as it mirrors another time-related observation.

Throughout the measurements it became apparent, that parallel DC81 and DC83 solar cells quickly decrease in performance following the measurement of surrounding cells. As seen in Figure 3.3, there are three individual cells on each substrate. The first measured cell always had the best parameters, with the others (and repeated measurements) dropping in performance until what seems to be a baseline of sorts is reached, even if the other cells were covered from light during the measurements. Their performance would however recover over time if left undisturbed, and after the first measurement the baseline would rise, although the behaviour would remain constant through the lifetime of the cell. An example of this is presented in Table 4.6. This behaviour is not only unfavourable for the use of DC81 and DC83 in solar cells, but may also have caused inaccuracies in results obtained from their measurements. If a measurement could not be completed on the first attempt due to for example bad contact, the second attempt would result in decreased performance. Alternatively, one may consider this "worn out" state of these cells to be their true capability.

As mentioned earlier and seen in Figure 4.7a, longer periods of time without measurements on the other hand seem to cause a notable increase in performance for devices employing DC81 and DC83, which then deteriorates as measurements become more frequent. Unlike the deterioration after measurements, this phenomenon was observed with all samples in batch 5, as they were not measured on the first day. With the properties of these HTMs being so linked to variation in time, it may provide more applicable information to instead utilize maximum power point tracking to characterize their stability in a continuous measurement. If one is interested in simulating a day/night cycle for the cell,

the MPP tracking may also be performed for example in 12-hour cycles of illumination and rest.

5. CONCLUSIONS

This thesis was carried out in the Hybrid Solar Cells team at Tampere University (TAU), with the aim of studying the suitability of four novel organic hole transfer materials, DC77, DC79, DC81, and DC83 in perovskite solar cells. The used device structure was glass/c-TiO$_2$/m-TiO$_2$/CsMAFA/HTM/Au, with Spiro-OMETAD doped with FK209, tBP, and Li-TFSI used as a reference. Additionally, the hole mobility, conductivity, hydrophobicity, as well as the optical and photophysical properties of the DC-HTMs were evaluated separately.

A consistent trend was observed throughout the experiments: DC77 and DC79 performed better in all experiments than the fluorine-based DC81 and DC83. The highest undoped solar cell efficiency was 13.9 % with a DC77-based device, in contrast to the reference cell showing a maximum PCE of 20.0 %. The average PCEs were 17.4 %, 10.8 %, 10.4 %, 7.8 %, and 7.6 % for cells employing Spiro-OMeTAD, DC77, DC79, DC81, and DC83 respectively. Comparing devices based on DC77 and DC79 to the doped Spiro-OMeTAD reference cells, the difference in average J_{SC} and V_{OC} was relatively small, but a great difference was observed in the FF. The average fill factor of the devices employing Spiro-OMeTAD was 67.9 %, while cells containing DC77 and DC79 attained only 52.5 % and 50.5 %, respectively. The shunt and series resistances of the DC champion cells were also worse than Spiro-OMeTAD cells, as was the case with their quantum efficiencies. This implies some internal efficiency losses.

The difference in fill factor may be explained at least partially by the significantly lower hole mobilities and conductivities of the DC-HTMs, which are known to reduce FF. Spiro-OMeTAD had a hole mobility of $4.9 \cdot 10^{-4} \, \text{cm}^2 \, \text{V}^{-1} \, \text{s}^{-1}$, while the DC-HTMs were in the range of $10^{-5} \, \text{cm}^2 \, \text{V}^{-1} \, \text{s}^{-1}$. While the conductivity of the doped Spiro-OMeTAD could unfortunately not be measured, literature values would place it at several orders of magnitude higher than even the best performing DC77 at $1.5 \cdot 10^{-6} \, \text{S} \, \text{cm}^{-1}$.

The low charge transporting values were alleviated thanks to the thinner layers of the DC-HTMs, as was seen in cross-section images taken with a scanning electron microscope. Compared to the average Spiro-OMeTAD layer of 150 nm, the DC-HTMs were up to 90 nm. The DC-films were not uniform however, with the gold electrode touching the perovskite at some points, indicating that the HTM-perovskite interface was not entirely

favourable. Another factor that may have contributed to the generally low fill factors was the thickness of the mesoporous and compact TiO_2-layers that were nearly twice as thick as those reported in literature.

Despite these issues, DC77 and DC79 performed well in the photoluminescence tests, with similar quenching efficiencies to doped Spiro-OMeTAD. This would suggest that their energy levels are well aligned with the used triple-cation CsMAFA perovskite, although their time resolved photoluminescence took longer to decay. This implies that the hole extraction at the perovskite-HTM interface is slower with DC-HTMs than doped Spiro-OMeTAD. Another favourable quality of all the DC-HTMs was their water contact angles which were approximately $20°$ higher than doped Spiro-OMeTAD, indicating much better hydrophobicity.

Finally, the observation of solar cell stability revealed interesting behaviour for the DC-HTM devices. While solar cells using doped Spiro-OMeTAD are known to improve over a short period following their fabrication, the DC-cells kept improving for approximately one week, reaching up to 60 % increase in PCE. The mechanism behind this phenomenon would require further study. Thanks to this initial improvement, none of the DC-cells fell below 80 % of their initial efficiency during the over 140 days long observation period, unlike those based on Spiro-OMeTAD. Towards the end the DC-cells did however exhibit accelerated performance decay, which suggests that a longer monitoring period may be needed to thoroughly evaluate their shelf-lifetimes.

In conclusion, the performance of the DC-HTMs could not match doped Spiro-OMeTAD, and suitable dopants may serve to bridge this gap caused by poor charge transportation of the intrinsic materials. Additionally, as DC77 and DC79 had good charge extraction properties, they may be suitable for p-i-n structure solar cells, where a thin hole transport layer is preferable. Thus, there are still some avenues worth exploring for these materials.

REFERENCES

[1] *Directive (EU) 2018/2001 of The European Parliament and of the Council. 11 December 2018. On the promotion of the use of energy from renewable sources.* URL: `https://eur-lex.europa.eu/legal-content/EN/TXT/PDF/?uri=CELEX:32018L2001&from=EN` (visited on 09/04/2021).

[2] Schiermeier, Q., Tollefson, J., Scully, T., Witze, A. and Oliver, M. Energy alternatives: Electricity without carbon. *Nature* 454 (2008), pp. 816–823. DOI: `10.1038/454816a`.

[3] *Key World Energy Statistics 2020.* URL: `https://www.iea.org/reports/key-world-energy-statistics-2020` (visited on 09/04/2021).

[4] Rathore, N., Panwar, N. L., Yettou, F. and Gama, A. A comprehensive review of different types of solar photovoltaic cells and their applications. *International Journal of Ambient Energy* 42.10 (2021), pp. 1200–1217. DOI: `10.1080/01430750.2019.1592774`.

[5] *Best Research-Cell Efficiency Chart. Emerging PV.* URL: `https://www.nrel.gov/pv/cell-efficiency.html` (visited on 07/26/2021).

[6] Saga, T. Advances in crystalline silicon solar cell technology for industrial mass production. *NPG Asia Materials* 2 (2010), pp. 96–102. DOI: `https://doi.org/10.1038/asiamat.2010.82`.

[7] Häberlin, H. Photovoltaics: System Design and Practice. 1st ed. John Wiley & Sons, Incorporated, 2012. Chap. 3 Solar Cells: Their Design Engineering and Operating Principles.

[8] Mertens, K. Photovoltaics: Fundamentals, Technology, and Practice. 2nd ed. John Wiley & Sons, Incorporated, 2018. Chap. 3 Fundamentals of Semiconductor Physics.

[9] Yoo, S., Domercq, B. and Kippelen, B. Intensity-dependent equivalent circuit parameters of organic solar cells based on pentacene and C60. *Journal of Applied Physics* 97.10 (2005), p. 103706. DOI: `10.1063/1.1895473`.

[10] Dennler, G., Forberich, K., Scharber, M. C., Brabec, C. J., Tomiš, I., Hingerl, K. and Fromherz, T. Angle dependence of external and internal quantum efficiencies in bulk-heterojunction organic solar cells. *Journal of Applied Physics* 102.5 (2007), p. 054516. DOI: `10.1063/1.2777724`.

[11] Watthage, S. C., Song, Z., Phillips, A. B. and Heben, M. J. Chapter 3 - Evolution of Perovskite Solar Cells. *Perovskite Photovoltaics*. Ed. by S. Thomas and A. Thankappan. Academic Press, 2018, pp. 43–88. ISBN: 978-0-12-812915-9. DOI: `https://doi.org/10.1016/B978-0-12-812915-9.00003-4`.

[12] Green, M., Ho-Baillie, A. and Snaith, H. The emergence of perovskite solar cells. *Nature Photonics* 8 (2014), pp. 506–514. DOI: `10.1038/nphoton.2014.134`.

[13] Kojima, A., Teshima, K., Miyasaka, T. and Yasuo, S. Novel Photoelectrochemical Cell with Mesoscopic Electrodes Sensitized by Lead-Halide Compounds (2). *210th ECS Meeting* Abstract #397 (2006). DOI: `10.1149/ma2006-02/7/397`.

[14] Kojima, A., Teshima, K., Shirai, Y. and Miyasaka, T. Organometal Halide Perovskites as Visible-Light Sensitizers for Photovoltaic Cells. *Journal of the American Chemical Society* 131.17 (2009). PMID: 19366264, pp. 6050–6051. DOI: `10.1021/ja809598r`.

[15] Min, H., Lee, D. Y., Kim, J., Kim, G., Lee, K. S., Kim, J., Paik, M. J., Kim, Y. K., Kim, K. S., Kim, M. G., Shin, T. J. and Il Seok, S. Perovskite solar cells with atomically coherent interlayers on SnO2 electrodes. *Nature* 598 (2021), pp. 444–450. DOI: `10.1038/s41586-021-03964-8`.

[16] Rajagopal, A., Yao, K. and Jen, A. K.-Y. Toward Perovskite Solar Cell Commercialization: A Perspective and Research Roadmap Based on Interfacial Engineering. *Advanced Materials* 30.32 (2018), p. 1800455. DOI: `https://doi.org/10.1002/adma.201800455`.

[17] Wu, T., Qin, Z., Wang, Y., Wu, Y., Chen, W., Zhang, S., Cai, M., Dai, S., Zhang, J., Liu, J., Zhou, Z., Liu, X., Segawa, H., Tan, H., Tang, Q., Fang, J., Li, Y., Ding, L., Ning, Z., Qi, Y., Zhang, Y. and Han, L. The Main Progress of Perovskite Solar Cells in 2020–2021. *Nano-Micro Letters* 13.152 (2021). DOI: `doi.org/10.1007/s40820-021-00672-w`.

[18] Xiang, W., Liu, S. (and Tress, W. A review on the stability of inorganic metal halide perovskites: challenges and opportunities for stable solar cells. *Energy Environ. Sci.* 14 (4 2021), pp. 2090–2113. DOI: `10.1039/D1EE00157D`.

[19] Fu, Q., Tang, X., Huang, B., Hu, T., Tan, L., Chen, L. and Chen, Y. Recent Progress on the Long-Term Stability of Perovskite Solar Cells. *Advanced Science* 5.5 (2018), p. 1700387. DOI: `https://doi.org/10.1002/advs.201700387`.

[20] Berry, J., Buonassisi, T., Egger, D. A., Hodes, G., Kronik, L., Loo, Y.-L., Lubomirsky, I., Marder, S. R., Mastai, Y., Miller, J. S., Mitzi, D. B., Paz, Y., Rappe, A. M., Riess, I., Rybtchinski, B., Stafsudd, O., Stevanovic, V., Toney, M. F., Zitoun, D., Kahn, A., Ginley, D. and Cahen, D. Hybrid Organic–Inorganic Perovskites (HOIPs): Opportunities and Challenges. *Advanced Materials* 27.35 (2015), pp. 5102–5112. DOI: `https://doi.org/10.1002/adma.201502294`.

[21] Babayigit, A., Ethirajan, A., Muller, M. and Conings, B. Toxicity of organometal halide perovskite solar cells. *Nature materials* 15 (2016), pp. 247–251. DOI: `doi.org/10.1038/nmat4572`.

[22] Jiang, X., Li, H., Zhou, Q., Wei, Q., Wei, M., Jiang, L., Wang, Z., Peng, Z., Wang, F., Zang, Z., Xu, K., Hou, Y., Teale, S., Zhou, W., Si, R., Gao, X., Sargent, E. H. and Ning, Z. One-Step Synthesis of SnI2·(DMSO)x Adducts for High-Performance Tin

Perovskite Solar Cells. *Journal of the American Chemical Society* 143.29 (2021), pp. 10970–10976. DOI: `10.1021/jacs.1c03032`.

[23]   Manjunath, V., Krishna, R., Maniarasu, S., Ramasamy, E., Shanmugasundaram, S. and Veerappan, G. Chapter 4 - Perovskite Solar Cell Architectures. *Perovskite Photovoltaics*. Ed. by S. Thomas and A. Thankappan. Academic Press, 2018, pp. 89–121. ISBN: 978-0-12-812915-9. DOI: `https://doi.org/10.1016/B978-0-12-812915-9.00004-6`.

[24]   Mohamad Noh, M. F., Teh, C. H., Daik, R., Lim, E. L., Yap, C. C., Ibrahim, M. A., Ahmad Ludin, N., Mohd Yusoff, A. R. b., Jang, J. and Mat Teridi, M. A. The architecture of the electron transport layer for a perovskite solar cell. *J. Mater. Chem. C* 6 (4 2018), pp. 682–712. DOI: `10.1039/C7TC04649A`.

[25]   Sze, S. M. *Physics of semiconductor devices*. 2nd ed. John Wiley & Sons, Incorporated, 1981, pp. 27–31. ISBN: 0-471-05661-8.

[26]   Stolterfoht, M., Wolff, C. M., Amir, Y., Paulke, A., Perdigón-Toro, L., Caprioglio, P. and Neher, D. Approaching the fill factor Shockley–Queisser limit in stable, dopant-free triple cation perovskite solar cells. *Energy Environ. Sci.* 10 (6 2017), pp. 1530–1539. DOI: `10.1039/C7EE00899F`.

[27]   Le Corre, V. M., Stolterfoht, M., Perdigón Toro, L., Feuerstein, M., Wolff, C., Gil-Escrig, L., Bolink, H. J., Neher, D. and Koster, L. J. A. Charge Transport Layers Limiting the Efficiency of Perovskite Solar Cells: How To Optimize Conductivity, Doping, and Thickness. *ACS Applied Energy Materials* 2.9 (2019), pp. 6280–6287. DOI: `10.1021/acsaem.9b00856`.

[28]   Kim, H.-S., Lee, C.-R., Im Jeong, H., Lee, K.-B., Moehl, T., Marchioro, A., Moon, S.-J., Humphry-Baker, R., Yum, J.-H., Moser, J. E., Grätzel, M. and Park, N.-G. Lead Iodide Perovskite Sensitized All-Solid-State Submicron Thin Film Mesoscopic Solar Cell with Efficiency Exceeding 9%. *Scientific Reports* 2 (591 2012). DOI: `10.1038/srep00591`.

[29]   Petrus, M. L., Bein, T., Dingemans, T. J. and Docampo, P. A low cost azomethine-based hole transporting material for perovskite photovoltaics. *J. Mater. Chem. A* 3 (23 2015), pp. 12159–12162. DOI: `10.1039/C5TA03046C`.

[30]   Rombach, F. M., Haque, S. A. and Macdonald, T. J. Lessons learned from spiro-OMeTAD and PTAA in perovskite solar cells. *Energy Environ. Sci.* 14 (10 2021), pp. 5161–5190. DOI: `10.1039/D1EE02095A`.

[31]   Li, W., Dong, H., Wang, L., Li, N., Guo, X., Li, J. and Qiu, Y. Montmorillonite as bifunctional buffer layer material for hybrid perovskite solar cells with protection from corrosion and retarding recombination. *J. Mater. Chem. A* 2 (33 2014), pp. 13587–13592. DOI: `10.1039/C4TA01550A`.

[32]   Hawash, Z., Ono, L. K., Raga, S. R., Lee, M. V. and Qi, Y. Air-Exposure Induced Dopant Redistribution and Energy Level Shifts in Spin-Coated Spiro-MeOTAD Films. *Chemistry of Materials* 27.2 (2015), pp. 562–569. DOI: `10.1021/cm504022q`.

[33] Wei, Z., Chen, H., Yan, K., Zheng, X. and Yang, S. Hysteresis-free multi-walled carbon nanotube-based perovskite solar cells with a high fill factor. *J. Mater. Chem. A* 3 (48 2015), pp. 24226–24231. DOI: 10.1039/C5TA07714A.

[34] Abdellah, I. M., Chowdhury, T. H., Lee, J.-J., Islam, A., Nazeeruddin, M. K., Gräetzel, M. and El-Shafei, A. Facile and low-cost synthesis of a novel dopant-free hole transporting material that rivals Spiro-OMeTAD for high efficiency perovskite solar cells. *Sustainable Energy Fuels* 5 (1 2021), pp. 199–211. DOI: 10.1039/D0SE01323D.

[35] Zhang, H., Liu, M., Yang, W., Judin, L., Hukka, T. I., Priimagi, A., Deng, Z. and Vivo, P. Thionation Enhances the Performance of Polymeric Dopant-Free Hole-Transporting Materials for Perovskite Solar Cells. *Advanced Materials Interfaces* 6.18 (2019), p. 1901036. DOI: https://doi.org/10.1002/admi.201901036.

[36] Oksana, O. Handbook of Organic Materials for Optical and (Opto)Electronic Devices : Properties and Applications. Vol. 39. Woodhead Publishing, 2013, pp. 384–388. ISBN: 9780857092656.

[37] Tabor, D. P., Chiykowski, V. A., Friederich, P., Cao, Y., Dvorak, D. J., Berlinguette, C. P. and Aspuru-Guzik, A. Design rules for high mobility xanthene-based hole transport materials. *Chem. Sci.* 10 (36 2019), pp. 8360–8366. DOI: 10.1039/C9SC01491H.

[38] Patane, A. and Balkan, N. Semiconductor Research: Experimental Techniques. Springer, Berlin, Heidelberg, 2012. Chap. 5 Photoluminscence: A Tool for Investigating Optical, Electronic, and Structural Properties of Semiconductors, pp. 125–133.

[39] Patane, A. and Balkan, N. Semiconductor Research: Experimental Techniques. Springer, Berlin, Heidelberg, 2012. Chap. 8 Time-Resolved Optical Spectroscopy, pp. 251–256.

[40] Law, K.-Y. and Zhao, H. Surface Wetting: Characterization, Contact Angle, and Fundamentals. 1st ed. Springer, Cham, 2016, pp. 7, 128. ISBN: 978-3-319-25214-8.

[41] Goldstein, J., Newbury, D. E., Joy, D. C., Lyman, C. E., Echlin, P., Lifshin, E., Sawyer, L. C. and Michael, J. *Scanning Electron Microscopy and X-ray Microanalysis*. 3rd ed. Springer, 2012, pp. 1–2. ISBN: 9781461502159.

[42] Petrus, M. L., Music, A., Closs, A. C., Bijleveld, J. C., Sirtl, M. T., Hu, Y., Dingemans, T. J., Bein, T. and Docampo, P. Design rules for the preparation of low-cost hole transporting materials for perovskite solar cells with moisture barrier properties. *J. Mater. Chem. A* 5 (48 2017), pp. 25200–25210. DOI: 10.1039/C7TA06452G.

[43] Pham, N. D., Shang, J., Yang, Y., Hoang, M. T., Tiong, V. T., Wang, X., Fan, L., Chen, P., Kou, L., Wang, L. and Wang, H. Alkaline-earth bis(trifluoromethanesulfonimide) additives for efficient and stable perovskite solar cells. *Nano Energy* 69 (2020), p. 104412. ISSN: 2211-2855. DOI: https://doi.org/10.1016/j.nanoen.2019.104412.

[44] Abate, A., Leijtens, T., Pathak, S., Teuscher, J., Avolio, R., Errico, M. E., Kirkpatrik, J., Ball, J. M., Docampo, P., McPherson, I. and Snaith, H. J. Lithium salts as "redox active" p-type dopants for organic semiconductors and their impact in solid-state dye-sensitized solar cells. *Phys. Chem. Chem. Phys.* 15 (7 2013), pp. 2572–2579. DOI: 10.1039/C2CP44397J.

[45] Ye, T., Wang, J., Chen, W., Yang, Y. and He, D. Improved Performance and Reproducibility of Perovskite Solar Cells by Well-Soluble Tris(pentafluorophenyl)borane as a p-Type Dopant. *ACS Applied Materials & Interfaces* 9.21 (2017), pp. 17923–17931. DOI: 10.1021/acsami.7b02969.

[46] Xu, B., Bi, D., Hua, Y., Liu, P., Cheng, M., Grätzel, M., Kloo, L., Hagfeldt, A. and Sun, L. A low-cost spiro[fluorene-9,9-xanthene]-based hole transport material for highly efficient solid-state dye-sensitized solar cells and perovskite solar cells. *Energy Environ. Sci.* 9 (3 2016), pp. 873–877. DOI: 10.1039/C6EE00056H.

[47] Wang, S., Huang, Z., Wang, X., Li, Y., Günther, M., Valenzuela, S., Parikh, P., Cabreros, A., Xiong, W. and Meng, Y. S. Unveiling the Role of tBP–LiTFSI Complexes in Perovskite Solar Cells. *Journal of the American Chemical Society* 140.48 (2018), pp. 16720–16730. DOI: 10.1021/jacs.8b09809.

[48] Zheng, L., Chung, Y.-H., Ma, Y., Zhang, L., Xiao, L., Chen, Z., Wang, S., Qu, B. and Gong, Q. A hydrophobic hole transporting oligothiophene for planar perovskite solar cells with improved stability. *Chemical Communications* 50 (76 2014), pp. 11196–11199. DOI: 10.1039/C4CC04680C.

[49] Saliba, M., Correa-Baena, J.-P., Wolff, C. M., Stolterfoht, M., Phung, N., Albrecht, S., Neher, D. and Abate, A. How to Make over 20% Efficient Perovskite Solar Cells in Regular (n–i–p) and Inverted (p–i–n) Architectures. *Chemistry of Materials* 30.13 (2018), pp. 4193–4201. DOI: 10.1021/acs.chemmater.8b00136.

[50] Hawash, Z., Ono, L. K. and Qi, Y. Moisture and Oxygen Enhance Conductivity of LiTFSI-Doped Spiro-MeOTAD Hole Transport Layer in Perovskite Solar Cells. *Advanced Materials Interfaces* 3.13 (2016), p. 1600117. DOI: https://doi.org/10.1002/admi.201600117.